



UNIVERSITY  
OF TRENTO - Italy

Department of Materials Engineering  
and Industrial Technologies

Doctoral School in Materials Engineering – XXIII cycle

A grayscale photograph of a complex laboratory instrument, likely a scanning electron microscope (SEM) or a similar high-vacuum analytical tool. The machine is composed of numerous cylindrical and rectangular components, with a dense network of cables and hoses connected to it. The lighting is dramatic, with strong highlights and deep shadows, emphasizing the metallic textures and complex geometry of the equipment.

# Elastic Properties of Textured Nanocrystalline Thin Films

Matteo Ortolani

December 2011

*Dedicated to my uncle, Alessio Dalla Libera.*

# Abstract

Polycrystalline thin films and coatings often show preferred orientation of grains and crystalline domains, and develop a residual stress state as an effect of the growth mechanisms. These features can be conveniently measured by means of non-contact and non-destructive X-ray diffraction. As the technique only measures a map of strains along selected directions, stress evaluation requires a suitable constitutive equation, where the expression of moduli can be far from trivial if texture effects are to be taken into account; additionally, a grain interaction model needs to be enforced to describe strain and stress distribution among grains in the aggregate, based on background assumptions.

Several grain interaction models are available from literature: usually, a model or a combination of them provides a good fit of experimental data; often however underlying hypotheses are too restrictive or require unavailable information on certain microstructural parameters, leading this approach to fail. For this reason an experimental method was developed, for the characterisation of elastic properties and residual stress in thin film components by means of X-ray diffraction during in-situ mechanical testing.

This thesis presents a review of major literature works describing grain interaction modelling in textured components, and their implementation in X-ray diffraction stress analysis procedures. Following, the method for experimental characterisation of thin film elastic properties is described in detail. Applications are presented in the final chapter, that illustrates selected case studies on electrodeposited coatings.





# Contents

<b>1</b>	<b>Introduction</b>	<b>1</b>
1.1	Deposited film microstructure . . . . .	2
1.1.1	The <i>Orientation Distribution Function</i> . . . . .	3
1.2	X-ray diffraction for film characterisation . . . . .	5
<b>2</b>	<b>Stress and texture relationships in films by means of XRD</b>	<b>9</b>
2.1	Grain interaction modelling for X-ray diffraction stress measurements	9
2.1.1	Crystalline texture . . . . .	12
2.1.1.1	Direction-independent models . . . . .	15
2.1.1.2	Direction-dependent models . . . . .	20
2.1.1.3	Modelling experimental data . . . . .	24
2.1.2	Morphological texture . . . . .	25
2.1.2.1	Modelling experimental data . . . . .	28
2.2	The QXrdTex software package . . . . .	30
2.3	Measuring elastic grain interaction . . . . .	33
2.3.1	XEC evaluation by curvature methods . . . . .	35
2.3.2	In-situ mechanical testing for XEC evaluation . . . . .	37
2.3.3	Effects of texture gradients . . . . .	41
<b>3</b>	<b>Methods and Materials</b>	<b>43</b>
3.1	Methods: X-ray diffraction analysis . . . . .	43

3.1.1	Four-point bending device for in-situ mechanical testing . . . . .	45
3.2	Materials: electrodeposited coatings . . . . .	46
3.2.1	The electrodeposition process . . . . .	48
3.2.2	Composite Nickel coatings . . . . .	50
<b>4</b>	<b>Stress and texture relationship in nanocomposite galvanic coatings</b>	<b>53</b>
4.1	Elastic properties characterisation in a pure Nickel coating . . . . .	54
4.2	Effect of nanoparticle precipitation on texture and residual stress state	60
4.3	Stress and texture gradients in electrodeposited Nickel on brass . . . . .	66
	<b>Bibliography</b>	<b>74</b>
<b>A</b>	<b>QXrdTex user manual</b>	<b>83</b>
A.1	Data files . . . . .	83
A.2	Custom classes . . . . .	85
A.2.1	Generic-purpose classes . . . . .	86
A.2.2	Physical data manipulation classes . . . . .	90
A.3	Example script . . . . .	93

# Chapter 1

## Introduction

Thin films and coatings technology is among the major topics of research in materials science and engineering. Films are used to alter or enhance surface properties, providing protection from the working environment as well as additional features to the component. Microelectronics make extensive use of thin films as electronic circuit elements; this industry has occupied a leading position in the technological advancement of the last decades, and constitutes a major driving force in surface engineering research.

Thin films and coatings are often described as “two-dimensional” objects, thanks to their thickness to spread ratio. The film is grown for a limited thickness, and thus surface effects have a major impact on the final properties of the object. Moreover, growth is directional and occurs along specific paths, while on average perpendicularly to the substrate interface; as a consequence, films are likely to display transverse anisotropy, with properties changing significantly from in-plane to transverse direction. This effect can be either beneficial or detrimental to the component applications, and as such needs to be carefully investigated.

It is important to note that deposition conditions, much more than interactions at the substrate interface, determine the final structure of a film component, and hence its properties. For this reason, accurate characterisation of microstructure and properties relationships is imperative to devise the most convenient deposition setup, in order to achieve the required features in the final coated component.

**On grains and crystalline domains** In the following paragraphs, both grains and crystallites (or crystalline domains) will be mentioned. It is therefore worth to define these entities as follows, in order to avoid confusion. Hereafter, *crystallite* indicates a region within a single phase where the crystalline lattice is continuous and uniformly oriented; its boundaries are defined by discontinuities in the periodic atomic structure. The term *grain* is instead used to indicate a portion of a phase that originates from the same nucleus; its boundaries are defined by the (generally amorphous) layers formed where two growing fronts encounter or by physical boundaries, such as a mould's walls. While the two terms are generally interchangeable, the opposite may also occur; a grain can, for instance, comprise several crystallites that originate from the same nucleus.

## 1.1 Deposited film microstructure

Film morphology, as in grain size and orientation, mainly depends on the choice of deposition technique and working conditions; different mechanisms can activate and control growth as a function of processing parameters. Additionally, substrate choice and final thickness of the deposit are also known to play a role in thin film microstructure definition.

**Morphology and structure-zone diagrams** Morphology has been historically classified into structure-zone diagrams (SZD) [1], the most simple of which define temperature ranges (in terms of growing surface to melting temperature ratio) in which certain microstructures are expected to be found. Description can be enhanced by a larger number of parameters, such as final thickness or deposition chamber gas pressure, increasing the number of dimensions required to draw the structure-zone diagram (see Figure 1.1 for a qualitative example). While a complete treatise on this topic goes beyond the scope of this thesis, it is worth to keep in mind how deposition structures are categorised for reference purposes.

**Crystallographic texture** On top of glaring morphological features, deposited films often display peculiar crystallographic features. Often directional growth leads

### 1.1. Deposited film microstructure

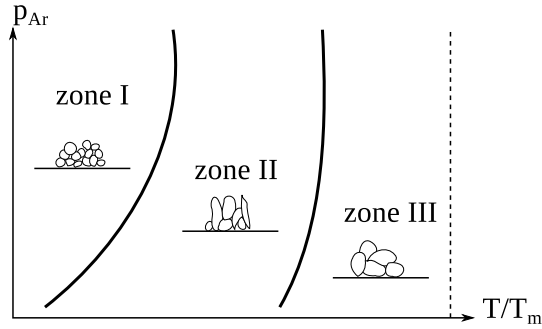


Figure 1.1: Structure-zone diagram, indicating a sputtered film morphology as a function of deposition parameters (growing surface temperature and sputtering gas pressure).

to preferred crystallites orientation, or crystalline *texture*, with certain atomic planes rather being stacked along the normal to the film surface.

In the most general case, preferred orientation is identified by a plane-direction pair. For example, a rolled metal sheet may display a deformation texture, arising from dislocation slip and grain rotation, identified as  $(110)[111]$ : meaning that  $(110)$  planes are preferably found in the sheet plane and  $[111]$  directions are mainly aligned to the rolling direction. Thin films on the other hand are likely to display rotational in-plane symmetry; this because hardly anything discriminates in-plane directions in a polycrystalline deposit. As a consequence, textures are often only indicated by means of one plane family, indicating one that is most often found parallel to the surface.

Like morphological features, crystallographic texture may also be referred to in structure-zone diagrams.

#### 1.1.1 The *Orientation Distribution Function*

Texture, either crystallographic or morphological, can be described using an *orientation distribution function* (ODF), hereby indicated as  $f$ . The function returns the density of crystallites (or grains) whose principal axes are rotated in a fashion described by the function arguments, in respect to the object's reference frame. For ex-

ample,  $f$  can be written as a function of three Eulerian angles: in this work, this form will be preferred, and the Roe [2] notation will be used (with  $\alpha = \Psi$ ,  $\beta = \Theta$ ,  $\gamma = \Phi$ ). In this description, the complete rotation reads as follows:

1. rotate around  $x_3^S$  by  $\alpha$ : transformation from the  $S$  (sample) reference frame to  $S'$
2. rotate around  $x_2^{S'}$  by  $\beta$ : transformation from  $S'$  to  $S''$
3. rotate around  $x_3^{S''}$  by  $\gamma$ : transformation from  $S''$  to  $S''' \equiv C$  (crystal)

The angle triad can be conveniently written in the form of a vector,  $\mathbf{g} = (\alpha, \beta, \gamma)$ . The Euler space, containing all the possible  $\mathbf{g}$  vectors, is finite and bound within  $0 \leq \alpha, \gamma < 2\pi$  and  $0 \leq \beta < \pi$ . The volume element in this space is  $d^3\mathbf{g} = d\alpha \sin \beta d\beta d\gamma$  [3, 2]; integrating,

$$\int_0^{2\pi} d\alpha \int_0^\pi \sin \beta d\beta \int_0^{2\pi} d\gamma = \iiint_G d\mathbf{g} = 8\pi^2 \quad (1.1)$$

As a consequence, a normalisation condition naturally follows, that is applied enforcing  $\iiint_G f(\mathbf{g}) d\mathbf{g} = 8\pi^2$ .

The orientation distribution function possesses, under commonly encountered circumstances, several axes of symmetry. This leads to simplifications in the function expression, as well as allowing shorter data collection time when the ODF needs to be measured.

**Unit cell symmetry** In crystalline texture, unit cell symmetry is reflected in the ODF, allowing a narrower angle range to be representative of the whole data array. As an example, let us assume we are describing the orientation distribution function of a polycrystal with a cubic unit cell. In the cubic system, any  $(h00)$  is a plane of symmetry. Hence, a  $\pi - \beta$  rotation is equivalent to a  $\beta$  rotation; similarly, a  $\pi \pm \gamma$  rotation is equivalent to a  $\gamma$  rotation and so is  $2\pi - \gamma$ . This means that the  $[0, \pi/2]$  interval is representative of the whole Euler space for a cubic system, for all three Euler angles. Equivalent arguments can be formulated for other crystalline symmetries.

## 1.2. X-ray diffraction for film characterisation

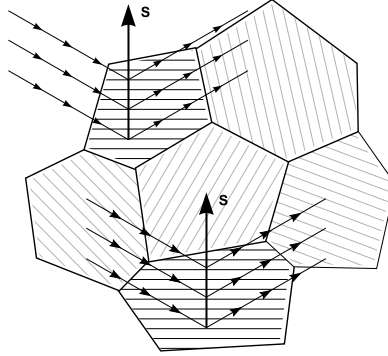


Figure 1.2: Diffraction from a polycrystalline aggregate. Non diffracting crystallites have been greyed out.

**ODF-weighted average** In a textured aggregate of individually anisotropic grains, physical properties vary as a function of direction within the sample. If single-crystal properties are available, macroscopic average can be calculated from texture data, by performing an ODF-weighted average over the whole Euler space. If the single-crystal property tensor is indicated as  $P$ , and the macroscopic average using angular brackets, as  $\langle P \rangle$ , we can write

$$\langle P \rangle = \iiint_G f(\mathbf{g}) P(\mathbf{g}) d\mathbf{g} \quad (1.2)$$

where the  $\mathbf{g}$  dependence of  $P$  indicates that the property needs to be rotated by the given Euler angles for the purpose of averaging.

## 1.2 X-ray diffraction for film characterisation

As already hinted, X-ray diffraction is a very convenient tool for characterisation of thin film structures, thanks to its non-contact and non-destructive nature [4]. Diffraction only detects a signal from crystallites whose atomic planes are suitably aligned to the beam path, the scattering planes normal to the bisector of the beam path, as shown in Figure 1.2.

It naturally follows that different information is acquired by tilting the sample around given angles (such as  $\phi$  rotation and  $\psi$  tilt, shown in Figure 1.3). In other words, it

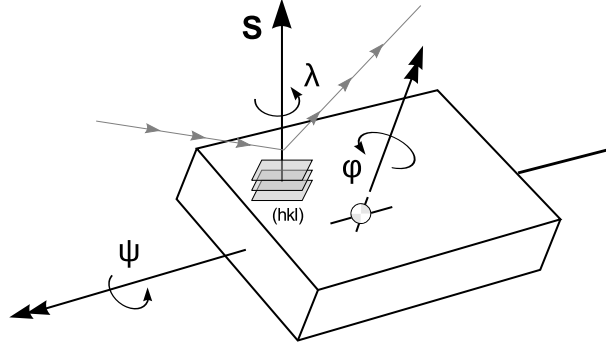


Figure 1.3: Sample to laboratory reference frame transformation

is possible to discriminate results as a function of direction within the sample; yet, it should be noted that information is nonetheless acquired as an average over all possible  $\lambda$  crystallite rotations around the scattering vector. If we indicate the  $P$  property average over this space with curly brackets as  $\{P\}$ :

$$\{P\} = \int_0^{2\pi} d\lambda P(hkl, \lambda, \phi, \psi) \quad (1.3)$$

When texture is present, it needs to enter the property average over the diffraction space and the result appropriately normalised, as hereby shown:

$$\{P\} = \frac{\int_0^{2\pi} d\lambda f^*(hkl, \lambda, \phi, \psi) P(hkl, \lambda, \phi, \psi)}{\int_0^{2\pi} d\lambda f^*(hkl, \lambda, \phi, \psi)} \quad (1.4)$$

A suitable coordinate transformation is required to provide the correct  $(\alpha, \beta, \gamma)$  arguments to the ODF, in terms of the X-ray diffraction setup parameters  $(hkl, \lambda, \phi, \psi)$ . This is guaranteed to be possible by the fact that only simple rotations are used in a diffraction experiment, and thus equivalent Euler angles (which cover all possible rotations in space) can be found. When the ODF is given in terms of diffraction parameters, the  $f^*$  symbol is used, to indicate that a coordinate conversion is required.

**XRD texture measurements** As an immediate application, crystallographic texture can be easily measured by diffraction. Information is given in terms of diffraction



## 1.2. X-ray diffraction for film characterisation

peak intensity, which is a function of the number of scattering planes, that in turn changes with sample rotation.

When the sample is rotated, or the beam incident angle is changed, different crystallite groups will be involved in producing a coherent signal from diffraction. In a randomly oriented powder, the diffraction peak intensity is expected to be identical at every sample rotation; the same does not hold true for a textured polycrystal, where diffraction peak intensity will show up as a function of  $\phi$  and  $\psi$  for a given  $hkl$  reflection; the  $I_{hkl}$  intensity as a function of  $(\phi, \psi)$  is conventionally called a *pole figure*. Different  $hkl$  plane families will return unique pole figures, that can be employed in reconstructing the whole ODF. Since peak intensity is proportional to the (square) number of scattering planes [5], it immediately follows that a single pole figure intensity can be expressed as the integral average of the ODF over the diffraction space, that is

$$I_{hkl}(\phi, \psi) = \frac{1}{2\pi} \int_0^{2\pi} d\lambda f^*(hkl, \lambda, \phi, \psi) \quad (1.5)$$

**Fibre texture in thin films** It has already been mentioned that polycrystalline thin films and coatings are expected to display rotational symmetry around the axis normal to their surface, as there is often no reason for properties to vary across different in-plane directions. Hence, textured polycrystalline films often show what is called a *fibre* texture, that is their orientation distribution function possesses an axis of symmetry that coincides with the normal to the sample surface.

This has an immediate practical application: pole figures are independent on  $\phi$ , thanks to rotational symmetry, hence the XRD measurement time can be drastically reduced. Rotational symmetry also means that the orientation distribution function  $f$  is independent on the first Euler angle in the Roe notation, or  $\partial f / \partial \alpha = 0$  (in fact, for the  $[h00]$  direction,  $\alpha \equiv \phi$ ); this allows the ODF expression to be significantly simplified.

*Chapter 1. Introduction*

## Chapter 2

# Stress and texture relationships in films by means of XRD

Thin films and coatings have been introduced as two-dimensional object, their thickness being orders of magnitude smaller than spread in the other two directions. This feature affects elastic properties, as it is likely to cause anisotropy between the in-plane and normal to the surface directions; and introduces constraints on the stress state, as any assumption such as “far enough from the surface” is clearly not applicable [6]. This chapter briefly illustrates the stress measurement technique by means of X-ray diffraction, then moves on to describing the literature models that can be applied to data analysis. Finally, weaknesses in literature models will be shown, and a new method for simultaneous experimental measurement of thin film elastic constants and residual stress state will be introduced.

### 2.1 Grain interaction modelling for X-ray diffraction stress measurements

As already mentioned, X-ray diffraction is often and conveniently used for residual stress characterisation, thanks to its non-contact and non-destructive nature [4]. The most important feature is that diffraction measures strains along one direction, in a

specific crystallite subset (see Figure 1.2). This constitutes a further complication to the stress characterisation problem, as it requires an *ad hoc* constitutive equation to produce a result. For this reason, proper modelling of elastic properties is critical to the technique's success.

Strains are measured along the scattering vector, in the diffractometer (or laboratory) frame of reference (henceforth indicated with a  $L$  superscript), whose  $x_3^L$  axis lies along said scattering vector; only crystallites whose scattering planes lay in the  $x_1^L x_2^L$  plane produce coherent diffraction. The XRD strain can then be written as

$$\{\varepsilon_{33}^L\}(hkl, \phi, \psi) = \int_0^{2\pi} d\lambda \varepsilon_{33}^L(hkl, \lambda, \phi, \psi) \quad (2.1)$$

The constitutive equation for a single crystallite reads

$$\varepsilon_{ij} = S_{ijkl} \sigma_{kl} \quad (2.2)$$

where  $S_{ijkl}$  is the single crystal compliance, and  $\sigma_{kl}$  the stress acting on the single crystallite. Defining the latter is no simple task; in fact, the stress in a single crystal is usually written as a function of the macroscopic average stress and a *grain interaction tensor*  $\Upsilon$ :

$$\sigma_{ij} = \Upsilon_{ijkl}(hkl, \lambda, \phi, \psi) \langle \sigma_{kl} \rangle \quad (2.3)$$

$\Upsilon$  is a mathematical representation of *a priori* hypotheses on stress distribution among crystallites; more information on the latter term is offered in the following paragraphs.

The ultimate result to be sought is the macroscopic average stress  $\langle \sigma_{kl} \rangle$ . In order to produce a constitutive equation that relates XRD strain to macroscopic average stress, the fourth-rank tensor  $A$  is introduced [7], combining Equations 2.2 and 2.3:

$$A_{33kl}^L = \int_0^{2\pi} d\lambda \Upsilon_{ijkl}^L(hkl, \lambda, \phi, \psi) \Omega_{mi}^{L \leftarrow C} \Omega_{nj}^{L \leftarrow C} S_{33mn}^C \quad (2.4)$$

Note the reference frame specifications: the integral average is performed in the diffraction frame of reference, whose  $x_3^L$  axis is aligned with the scattering vector. Single crystal compliance is rotated from the crystal ( $C$ ) to the laboratory ( $L$ ) frame of reference by means of the  $\Omega^{L \leftarrow C}$  rotation, which is a function of  $hkl$  and  $\lambda$ . Finally, the

### 2.1. Grain interaction modelling for X-ray diffraction stress measurements

constitutive equation for X-ray diffraction can be written as

$$\{\varepsilon_{ij}^L\} = A_{ijkl}^L \langle \sigma_{kl}^L \rangle \quad (2.5)$$

or, since only  $\{\varepsilon_{33}^L\}$  is effectively measured,

$$\{\varepsilon_{33}^L\} = A_{33kl}^L \langle \sigma_{kl}^L \rangle \quad (2.6)$$

Eventually, stress needs to be evaluated in the sample's frame of reference ( $S$  superscript), therefore the sample to laboratory transformation  $\Omega^{L \leftarrow S}$  is included. The latter transformation is usually expressed in terms of the angles  $\phi$  (sample rotation around  $x_3^S$ ) and  $\psi$  (sample tilt around  $x_2^S$ ), shown in Figure 1.3. Equation 2.6 becomes

$$\{\varepsilon_{33}^L\} = A_{33kl}^L \Omega_{km}^{L \leftarrow S} \Omega_{ln}^{L \leftarrow S} \langle \sigma_{mn}^S \rangle \quad (2.7)$$

The strain  $\{\varepsilon_{33}^L\}$  is a function of the sample to laboratory transformation ( $\phi$  and  $\psi$  angles) applied to the sample average stress tensor and also the  $hkl$  scattering plane family in the case of elastically anisotropic crystalline domains. Similarly, the elastic tensor  $A$  is a function of the single crystal elastic tensor,  $S^C$  and the plane family ( $hkl$ ). Where preferred orientation (texture) is present, the expression of  $A$  is further complicated by the introduction of two further parameters, the orientation distribution function ( $f$ ) and the grain interaction ( $\Upsilon$  tensor); this is more precisely described in the following Section. The complete expression for Equation 2.6 is then

$$\begin{aligned} \{\varepsilon_{33}^L\} (hkl, \phi, \psi) &= A_{33kl}^L (S^C, hkl, f, \Upsilon) \langle \sigma_{mn}^L \rangle (\phi, \psi) \\ &= A_{33kl}^L (S^C, hkl, f, \Upsilon) \Omega_{km}^{L \leftarrow S} (\phi, \psi) \Omega_{ln}^{L \leftarrow S} (\phi, \psi) \langle \sigma_{mn}^S \rangle \end{aligned} \quad (2.8)$$

Equation 2.8 is then often conveniently written using the so-called *stress factors* [8],  $F$ , which are the product of  $A$  and the sample to laboratory transformation:

$$F_{ij} = A_{33kl}^L \Omega_{ki}^{L \leftarrow S} \Omega_{lj}^{L \leftarrow S} \quad (2.9)$$

Equation 2.8 then becomes

$$\{\varepsilon_{33}^L\} (hkl, \phi, \psi) = F_{ij} (S^C, hkl, \phi, \psi, f, \Upsilon) \langle \sigma_{ij}^S \rangle \quad (2.10)$$

The constitutive equation is now formally written. X-ray elastic constants however were shown to depend on a parameter, grain interaction, which is a (usually unknown) description of how stresses are distributed among crystallites on the basis of *a priori* hypotheses. As several such hypotheses can be made, options will be illustrated in detail in the following paragraphs.

### 2.1.1 Crystalline texture

The most immediate grain interaction models apply to purely crystallographic descriptions, where only preferred orientation of crystallographic axes is taken into account, if present. Morphological features are not taken into account.

**Intrinsic elastic isotropy** In the case of a intrinsic elastic isotropy, i.e. a polycrystalline object composed of elastically isotropic crystallites, Equation 2.8 reduces to

$$\varepsilon_{33}^L = S_{33kl}^L \sigma_{kl}^L = \left( S_1 \delta_{kl} + \frac{1}{2} S_2 \delta_{3k} \delta_{3l} \right) \sigma_{kl}^L \quad (2.11)$$

where  $S_{ijkl}$  is the sample (but also single crystal) compliance tensor, with

$$S_1 = -\frac{\nu}{E} \text{ and } \frac{1}{2} S_2 = \frac{1+\nu}{E}$$

Note the absence of average indicators (curly brackets) as they become redundant under the given hypotheses; as crystallites show identical elastic behaviour, stresses and strains are expected to be the same throughout the whole aggregate. Again thanks to elastic isotropy,  $S$  applies to both the polycrystal and the single crystallite. For the same reason,  $\varepsilon_{33}^L$  no longer a function of  $hkl$ . Expanding the reference frame transformation in Equation 2.11 yields

$$\begin{aligned} \varepsilon_{33}^L(\phi, \psi) &= \frac{1}{2} S_2 \sin^2 \psi (\sigma_{11}^S \cos^2 \phi + \sigma_{12}^S \sin 2\phi + \sigma_{22}^S \sin^2 \phi) + \\ &+ \frac{1}{2} S_2 (\sigma_{13}^S \cos \phi \sin 2\psi + \sigma_{23}^S \sin \phi \sin 2\psi + \sigma_{33}^S \cos^2 \psi) \\ &+ S_1 (\sigma_{11}^S + \sigma_{22}^S + \sigma_{33}^S) \end{aligned} \quad (2.12)$$

which, for a planar stress state ( $\sigma_{11}^S = \sigma_{22}^S = \sigma_{\parallel}$ , whereas other components  $\sigma_{ij} = 0$ )

### 2.1. Grain interaction modelling for X-ray diffraction stress measurements

such as the one often found in thin layers and films, becomes

$$\varepsilon_{33}^L = \left( 2S_1 + \frac{1}{2} S_2 \sin^2 \psi \right) \sigma_{\parallel} \quad (2.13)$$

The latter equation shows why X-ray strain data is usually plotted as  $\varepsilon_{33}^L$  (sometimes as  $d_{hkl}$ ) against  $\sin^2 \psi$ , as the trend is linear for an elastically isotropic material and as such easily fitted to find  $\sigma_{\parallel}$ .

**Macroscopic elastic isotropy** Macroscopic elastic isotropy refers to a polycrystalline aggregate of randomly distributed elastically anisotropic crystallites, with direction-independent grain interaction (single crystal strain does not depend on its alignment in respect to the sample). Equation 2.8 can still be simplified in a fashion similar to Equation 2.11, albeit keeping the distinct averages over bulk and diffracting crystallites respectively and the dependence on  $hkl$  for  $\{\varepsilon^L\}$  and  $A$ . The latter tensor is written in terms of single crystallite compliance for a given  $hkl$  crystallographic orientation  $S(hkl)$

$$\begin{aligned} \{\varepsilon_{33}^L\} &= S_{33kl}(hkl) \langle \sigma_{kl}^L \rangle \\ &= \left( S_1(hkl) \delta_{kl} + \frac{1}{2} S_2(hkl) \delta_{3k} \delta_{3l} \right) \langle \sigma_{kl}^L \rangle \end{aligned} \quad (2.14)$$

Note that, in this case, the sample average remains indicated for the stress tensor. As will be shown later in greater detail, in calculating the  $hkl$ -dependent compliance, one may assume that either 1) all crystallites are subject to the same stress (in this case the sample average will disappear) or 2) all crystallite are subject to the same strain (Reuss and Voigt hypothesis, respectively); these have been proved to be the extremal cases within which a real material's behaviour is to be found [9].

Equation 2.14 can then be expanded to include the sample to laboratory reference frame transformation, in exactly the same fashion as Equation 2.12, and obtaining,

$$\begin{aligned} \varepsilon_{33}^L(\phi, \psi) &= \frac{1}{2} S_2(hkl) \sin^2 \psi (\langle \sigma_{11}^S \rangle \cos^2 \phi + \langle \sigma_{12}^S \rangle \sin 2\phi + \langle \sigma_{22}^S \rangle \sin^2 \phi) + \\ &+ \frac{1}{2} S_2(hkl) (\langle \sigma_{13}^S \rangle \cos \phi \sin 2\psi + \langle \sigma_{23}^S \rangle \sin \phi \sin 2\psi + \langle \sigma_{33}^S \rangle \cos^2 \psi) \\ &+ S_1(hkl) (\langle \sigma_{11}^S \rangle + \langle \sigma_{22}^S \rangle + \langle \sigma_{33}^S \rangle) \end{aligned} \quad (2.15)$$

Which, for a planar stress state ( $\langle \sigma_{11}^S \rangle = \langle \sigma_{22}^S \rangle = \sigma_{\parallel}$ ), becomes

$$\{\varepsilon_{33}^L\} = \left( 2S_1(hkl) + \frac{1}{2}S_2(hkl) \sin^2 \psi \right) \sigma_{\parallel} \quad (2.16)$$

We now define the so-called X-ray anisotropy factor  $\Gamma$  as

$$\Gamma = \frac{h^2 k^2 + h^2 l^2 + k^2 l^2}{(h^2 + k^2 + l^2)^2} \quad (2.17)$$

where  $3\Gamma$  varies between 0 (two zero indices) and 1 (three equal indices) for all possible families. It has been proved [10] that the X-ray diffraction strain measured on a reflection with  $3\Gamma = 0.6$  corresponds to the macroscopic mechanical strain: this is in fact the condition that makes the Reuss compliance (upper bound) equal to the Voigt compliance (lower bound). In other words, the macroscopic elastic compliance  $\langle S \rangle$  can be calculated by evaluating the elastic constants with  $3\Gamma = 0.6$ .

**Macroscopic elastic anisotropy** When a sample is made of elastically anisotropic crystallites with non-random orientation, the constitutive equation cannot be easily simplified as in the cases above, and stress factors assume more complicated expressions.

Single crystal compliance needs to be averaged over the whole space of possible rotations for crystallites, which is finite and includes a full revolution around the scattering vector. The ODF is used as a weight and a suitable grain interaction model ( $\Upsilon$  tensor) is enforced: remember that the stress state of a single crystallite is  $\sigma_{ij} = \Upsilon_{ijkl} \langle \sigma_{kl} \rangle$ , and therefore its strain is  $\varepsilon_{ij} = S_{ijkl} \Upsilon_{klmn} \langle \sigma_{mn} \rangle$ . It is worth to note that stress tensor symmetries reflect on the grain interaction tensor, hence  $\Upsilon_{ijkl} = \Upsilon_{jikl} = \Upsilon_{ijlk}$ . The diffraction average strain  $\{\varepsilon\}$  can then be obtained by averaging the strain in each crystallite  $\varepsilon$  over all possible  $\lambda$  rotations around the scattering vector, using the ODF as weight.



### 2.1. Grain interaction modelling for X-ray diffraction stress measurements

$$\begin{aligned}
 \{\varepsilon_{33}^L\} &= \frac{\int_0^{2\pi} \varepsilon_{33}^L f^* d\lambda}{\int_0^{2\pi} f^* d\lambda} \\
 &= \frac{\int_0^{2\pi} S_{33kl}^L \Upsilon_{klmn}^L \langle \sigma_{mn}^L \rangle f^* d\lambda}{\int_0^{2\pi} f^* d\lambda}
 \end{aligned} \tag{2.18}$$

Note that the reference frame transformation from the laboratory to each diffracting crystallite is a function of  $hkl$  and the  $\lambda$  rotation around the scattering vector; the product of such transformation with the already mentioned sample to laboratory rotation  $\Omega^{L \leftarrow S}$  returns a sample to crystal transformation. To the latter, a unique triad of Euler angles can be associated, thus allowing the ODF in Equation 2.18 to be effectively expressed as a function of the diffraction parameters as  $f^*(hkl, \lambda, \phi, \psi)$ .

One can also note that in Equation 2.18, the bulk average stress tensor  $\langle \sigma_{mn}^L \rangle$  is independent on  $hkl$  or  $\lambda$  and thus can be effectively taken out of the integral. The expression for the stress factors introduced in Equation 2.10 immediately follows

$$F_{ij}(hkl, \phi, \psi) = \frac{\int_0^{2\pi} S_{33kl}^L \Upsilon_{klij}^L f^* d\lambda}{\int_0^{2\pi} f^* d\lambda} \tag{2.19}$$

Grain interaction can be based on different hypotheses: under these premises, the expression for the  $\Upsilon$  tensor may change significantly, returning radically different elastic constant trends as a function of sample orientation. As an example, Figure 2.1 shows for the (200) family of a texture-free, pure Nickel polycrystal, the stress factors sum  $F_{11} + F_{22}$  as a function of  $\sin^2 \psi$ , which is but the ratio between XRD strain and in-plane stress; this has to be compared to the model for an elastically, intrinsically isotropic polycrystal, which is expected to display a linear trend.

#### 2.1.1.1 Direction-independent models

The first models to be presented were originally conceived for bulk rather than thin objects. They represent the most simple scenario, posing identical conditions for all directions in the polycrystal, which are assumed to be equivalent.

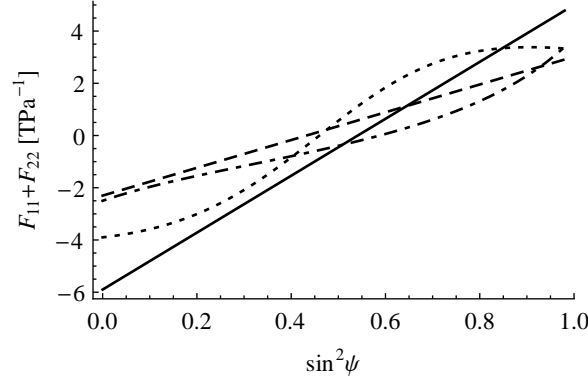


Figure 2.1: Stress factors ( $F_{11} + F_{22}$ ) as a function of  $\sin^2 \psi$  for a texture-free pure Nickel polycrystal, comparison of different grain interaction models: Reuss (solid line), Voigt (dashed line), Vook-Witt (dotted line) and inverse Vook-Witt (dashed-dotted line).

**Reuss** Under the Reuss hypothesis [11], grains are assumed to be subject to the same stress state, but can deform freely in all directions. Since  $\sigma = \langle \sigma \rangle$ , the grain interaction tensor  $\Upsilon$  is simply the fourth-rank identity tensor

$$\Upsilon_{ijkl} = I_{ijkl} = 1/2 (\delta_{ik}\delta_{jl} + \delta_{il}\delta_{jk}) \quad (2.20)$$

and the bulk constitutive equation can be written as

$$\langle \varepsilon_{ij} \rangle = \iiint_G S_{ijkl} \sigma_{kl} f(\mathbf{g}) d\mathbf{g} = \left[ \iiint_G S_{ijkl} f(\mathbf{g}) d\mathbf{g} \right] \langle \sigma_{kl} \rangle \quad (2.21)$$

with the stress tensor being taken out of the integral because of the original hypothesis,  $\sigma = \langle \sigma \rangle$ . The bulk average compliance  $\langle S \rangle$  can then be calculated as an ODF-weighted average of single crystal compliance  $S^C$  (see also Equation 1.2)

$$\langle S_{ijkl}^S \rangle = \iiint_G f(\mathbf{g}) \Omega_{im} \Omega_{jn} \Omega_{ko} \Omega_{lp} S_{mnop}^C d\mathbf{g} \quad (2.22)$$

with  $\Omega$  being the transformation matrix corresponding the Euler  $\mathbf{g}$  rotation, transforming the crystal reference frame into the sample's. It is worth to note that the constitutive equation (Equation 2.21) cannot be as easily written in terms of stiffness,

2.1. Grain interaction modelling for X-ray diffraction stress measurements

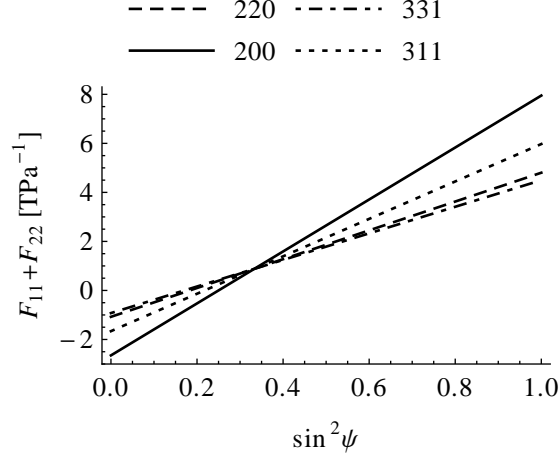


Figure 2.2: Untextured Ni, Reuss stress factors  $F_{11} + F_{22}$  versus  $\sin^2 \psi$  ( $\phi = 0$ ).

and that the average stiffness is not just the ODF-weighted average of single crystal stiffness. This means that the model is not self-consistent.

The Reuss stress factors expression then becomes

$$F_{ij}(hkl, \phi, \psi) = \frac{\int_0^{2\pi} S_{33ij}^L f^* d\lambda}{\int_0^{2\pi} f^* d\lambda} \quad (2.23)$$

where  $S^L$  is the single crystal elastic compliance, in the diffractometer ( $L$ ) reference frame; this rotation transformation is a function of  $\lambda$  and  $hkl$ , hence the final X-ray stress factors will be  $hkl$ -dependent. As an example, figure 2.2 shows  $F_{11} + F_{22}$  as a function of  $\sin^2 \psi$  for untextured Nickel, calculated with the Reuss model; note that they are linear versus  $\sin^2 \psi$ , but depend on  $hkl$  as expected.

**Voigt** In the Voigt hypothesis [12], grains are subject to an identical strain state, i.e.  $\varepsilon = \langle \varepsilon \rangle$ . The constitutive equation can be written as

$$\langle \sigma_{ij} \rangle = \iiint_G C_{ijkl} \varepsilon_{kl} f(\mathbf{g}) d\mathbf{g} = \left[ \iiint_G S_{ijkl} f(\mathbf{g}) d\mathbf{g} \right] \langle \varepsilon_{kl} \rangle \quad (2.24)$$

Similarly to the Reuss approach, the strain is taken out of the average as it is assumed

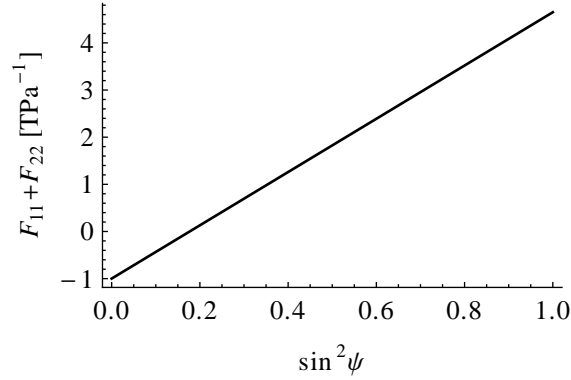


Figure 2.3: Untextured Ni, Voigt stress factors  $F_{11} + F_{22}$  versus  $\sin^2 \psi$  ( $\phi = 0$ ).

to be constant. Bulk average stiffness  $\langle C \rangle$  can be calculated as the ODF-weighted average of single crystal stiffness  $C$ , or

$$\langle C_{ijkl}^S \rangle = \iiint_G f(\mathbf{g}) \Omega_{im} \Omega_{jn} \Omega_{ko} \Omega_{lp} C_{mnop}^C d\mathbf{g} \quad (2.25)$$

Like in the Reuss case, the constitutive equation cannot be written as easily in terms of compliance. In fact, Voigt average stiffness is not the inverse of Reuss average compliance, neither model is self-consistent.

The macroscopic average Voigt compliance is calculated as  $\langle S \rangle = \langle C \rangle^{-1}$ . As  $\{\varepsilon\} = \langle \varepsilon \rangle = \langle S \sigma \rangle$ , X-ray stress factors can be expressed by means of a simple sample to laboratory transformation  $\Omega^{L \leftarrow S}$ , as in

$$F_{ij}(\phi, \psi) = \langle S_{33kl} \rangle \Omega_{ki}^{L \leftarrow S} \Omega_{lj}^{L \leftarrow S} \quad (2.26)$$

Note that, under these premises, stress factors do not depend on  $hkl$ . As an example, Figure 2.2 shows  $F_{11} + F_{22}$  as a function of  $\sin^2 \psi$  for untextured Nickel, as calculated with the Voigt model.

**Hill average** Hill proved that Reuss and Voigt models represent respectively the lower and upper bound for the elastic moduli of a macroscopic aggregate [9]. For this reason, the arithmetic average of the Voigt and Reuss results is often taken as an

### 2.1. Grain interaction modelling for X-ray diffraction stress measurements

approximation of the material's behaviour. Although not strictly a grain interaction model, as it does not enforce any hypothesis on stress or strain distribution, this technique has been labelled the Neerfeld-Hill model [13].

As an alternative to the arithmetic average, weighted average of Reuss and Voigt elastic constants can also be used. The weight parameter can be arbitrarily enforced, or it can be entered as a minimization parameter in fitting experimental points. This approach is often called Hill's weighted average.

**Geometric mean** The geometric mean is, again, not really a grain interaction model, much like the Hill description. Unlike Reuss and Voigt approaches, however, it offers a self-consistent alternative to the elastic constant calculation problem [14]. Elastic constants are averaged geometrically, instead of arithmetically and thus the geometric mean compliance is the inverse of the geometric mean stiffness.

In order to evaluate geometric average elastic constants, the single crystal elastic stiffness  $C$  is first written in matrix form, then its natural logarithm  $C^{\log}$  is computed, after diagonalization. The operation consists of computing the eigensystem for  $C$ ; eigenvalues will be indicated as  $\lambda_i$  and corresponding eigenvectors as  $\mathbf{q}_i$ . Now, if eigenvectors are arranged as columns in a matrix  $Q$  so that  $Q_{ij} = (\mathbf{q}_j)_i$ , and eigenvalues in a diagonal matrix  $\Lambda$  so that  $\Lambda_{ij} = \delta_{ij} \lambda_i$ , then  $C = Q\Lambda Q^{-1}$ . If we write a diagonal matrix  $\Lambda^{\log}$  whose elements are the logarithms of the eigenvalues, i.e.  $\Lambda_{ij}^{\log} = \delta_{ij} \log \lambda_i$ , then by definition,  $C^{\log} = \log C = Q\Lambda^{\log}Q^{-1}$ .

Since the logarithm of a product can be written as the sum of the logarithms of each term, the geometric mean can be calculated in the form of an integral mean. In fact, the ODF-weighted sample average of  $C^{\log}$  is calculated as shown in Equation 2.27:

$$\langle C_{ij}^{\log} \rangle = \iiint_G f(\mathbf{g}) \Omega_{ik} \Omega_{jl} C_{kl}^{\log} d\mathbf{g} \quad (2.27)$$

Eventually, the bulk average stiffness matrix will be  $\langle C_{ij} \rangle = \exp \langle C_{ij}^{\log} \rangle$ ; the matrix exponential is calculated in the same fashion as its logarithm, by computing its eigensystem and arranging now the exponential of eigenvalues in a diagonal matrix. The average compliance can finally be obtained by inverting the stiffness matrix,  $\langle S_{ij} \rangle = \langle C_{ij} \rangle^{-1}$ . Since the model is self-consistent, identical results will be obtained by performing the geometric average on the compliance tensor,  $S$ .

### 2.1.1.2 Direction-dependent models

Films are characterised by a very low thickness to spread ratio, and therefore under such premises equivalence of all directions in the sample is too loose an assumption. For this reason, direction dependent models have been proposed by Vook and Witt [15], based on the distinction between in-plane ( $x_1^S, x_2^S$ ) and out-of-plane ( $x_3^S$ ) directions.

**Vook-Witt** In the Vook-Witt assumption, crystallites are subject to identical in-plane strains, but can deform freely in the out-of-plane direction. Hence, for a transversely isotropic object under equibiaxial plane stress,  $\varepsilon_{11}^S = \varepsilon_{22}^S = \varepsilon_{\parallel}^S$  and  $\varepsilon_{12}^S = 0$  and  $\sigma_{13}^S = \sigma_{23}^S = \sigma_{33}^S = 0$ , whereas other components are unknown:

$$\varepsilon^S = \begin{pmatrix} \varepsilon_{\parallel}^S & 0 & \varepsilon_{13}^S \\ 0 & \varepsilon_{\parallel}^S & \varepsilon_{23}^S \\ \varepsilon_{13}^S & \varepsilon_{23}^S & \varepsilon_{33}^S \end{pmatrix} \quad \sigma = \begin{pmatrix} \sigma_{11}^S & \sigma_{12}^S & 0 \\ \sigma_{12}^S & \sigma_{22}^S & 0 \\ 0 & 0 & 0 \end{pmatrix} \quad (2.28)$$

Using matrix form, the constitutive equation for a single crystallite can be written as

$$\begin{pmatrix} \varepsilon_{\parallel}^S \\ \varepsilon_{\parallel}^S \\ \varepsilon_{33}^S \\ 2\varepsilon_{23}^S \\ 2\varepsilon_{13}^S \\ 0 \end{pmatrix} = \begin{pmatrix} S_{1111} & S_{1122} & S_{1133} & 2S_{1123} & 2S_{1113} & 2S_{1112} \\ S_{1122} & S_{2222} & S_{2233} & 2S_{2223} & 2S_{2213} & 2S_{2212} \\ S_{1133} & S_{2233} & S_{3333} & 2S_{3323} & 2S_{3313} & 2S_{3312} \\ 2S_{1123} & 2S_{2223} & 2S_{3323} & 4S_{2323} & 4S_{2313} & 4S_{2312} \\ 2S_{1113} & 2S_{2213} & 2S_{3313} & 4S_{2313} & 4S_{1313} & 4S_{1312} \\ 2S_{1112} & 2S_{2212} & 2S_{3312} & 4S_{2312} & 4S_{1312} & 4S_{1212} \end{pmatrix} \begin{pmatrix} \sigma_{11}^S \\ \sigma_{22}^S \\ 0 \\ 0 \\ 0 \\ \sigma_{12}^S \end{pmatrix} \quad (2.29)$$

Ruling out the 3<sup>rd</sup>, 4<sup>th</sup> and 5<sup>th</sup> row:

$$\begin{pmatrix} \varepsilon_{\parallel}^S \\ \varepsilon_{\parallel}^S \\ 0 \end{pmatrix} = \begin{pmatrix} S_{1111} & S_{1122} & 2S_{1112} \\ S_{1122} & S_{2222} & 2S_{2212} \\ 2S_{1112} & 2S_{2212} & 4S_{1212} \end{pmatrix} \begin{pmatrix} \sigma_{11}^S \\ \sigma_{22}^S \\ \sigma_{12}^S \end{pmatrix} \quad (2.30)$$

Equation 2.30 can be solved for  $(\sigma_{11}^S, \sigma_{22}^S, \sigma_{12}^S)$ , which will be expressed as a function of  $\varepsilon_{\parallel}^S$ . The last three unknowns ( $\varepsilon_{33}^S, 2\varepsilon_{23}^S, 2\varepsilon_{13}^S$ ) are obtained by solving remaining

## 2.1. Grain interaction modelling for X-ray diffraction stress measurements

equations:

$$\begin{pmatrix} \varepsilon_{33}^S \\ 2\varepsilon_{23}^S \\ 2\varepsilon_{13}^S \end{pmatrix} = \begin{pmatrix} S_{1133} & S_{2233} & 2S_{3312} \\ 2S_{1123} & 2S_{2223} & 4S_{2312} \\ 2S_{1113} & 2S_{2213} & 4S_{1312} \end{pmatrix} \begin{pmatrix} \sigma_{11}^S \\ \sigma_{22}^S \\ \sigma_{12}^S \end{pmatrix} \quad (2.31)$$

From the practical point of view, the whole operation of finding the unknown stress  $(\sigma_{11}^S, \sigma_{22}^S, \sigma_{12}^S)$  and strain  $(\varepsilon_{33}^S, 2\varepsilon_{23}^S, 2\varepsilon_{13}^S)$  components needs to be performed in every point in the Eulerian space, as the  $S$  matrix is rotated according to a given triad of angles. Once all unknowns are expressed in terms of the in-plane strain  $\varepsilon_{\parallel}^S$ , the latter can be assigned a virtual value. Bulk elastic constants may then be calculated as the ratio of the virtual  $\varepsilon_{\parallel}^S$  (or the calculated bulk average strain components) to the corresponding average stresses.

Stress factors evaluation follows a similar procedure. Bulk average stress components  $\langle \sigma_{ij} \rangle$  are calculated as a function of a known virtual strain  $\varepsilon_{\parallel}^S$ , by performing an ODF-weighted average of  $\sigma_{ij}$  over the whole Euler space (as in Equation 1.2). Then the average diffraction strain,  $\{\varepsilon_{33}^L\}$  is calculated using another ODF-weighted average over the diffracting crystallites subspace (Equation 1.4); finally,

$$F_{ij}(hkl, \phi, \psi) = \frac{\{\varepsilon_{33}^L\}}{\langle \sigma_{ij} \rangle} \quad (2.32)$$

It is worth to note, however, that the grain interaction tensor does not have a simple analytical expression for the Vook-Witt model.

Figure 2.4 shows the calculated  $F_{11} + F_{22}$  for untextured Nickel. Note the loss of linearity as a function of  $\sin^2 \psi$ , even in absence of preferred orientation.

**Inverse Vook-Witt** Taking an opposite approach from the Vook-Witt description, the inverse model [13, 6] assumes crystallites to be subject to an identical in-plane stress state, but tightly connected so that they exhibit identical out-of-plane strains. Under these assumptions, for a transversely isotropic object under equibiaxial plane stress, we fix  $\sigma_{11}^S = \sigma_{22}^S = \sigma_{\parallel}^S$ ,  $\sigma_{12}^S = 0$ ;  $\varepsilon_{33}^S = \varepsilon_{\perp}$ ,  $\varepsilon_{13}^S = \varepsilon_{23}^S = 0$ , i.e.

$$\varepsilon^S = \begin{pmatrix} \varepsilon_{11}^S & \varepsilon_{12}^S & 0 \\ \varepsilon_{12}^S & \varepsilon_{22}^S & 0 \\ 0 & 0 & \varepsilon_{\perp}^S \end{pmatrix} \quad \sigma = \begin{pmatrix} \sigma_{\parallel}^S & 0 & \sigma_{13}^S \\ 0 & \sigma_{\parallel}^S & \sigma_{23}^S \\ \sigma_{13}^S & \sigma_{23}^S & \sigma_{33}^S \end{pmatrix} \quad (2.33)$$

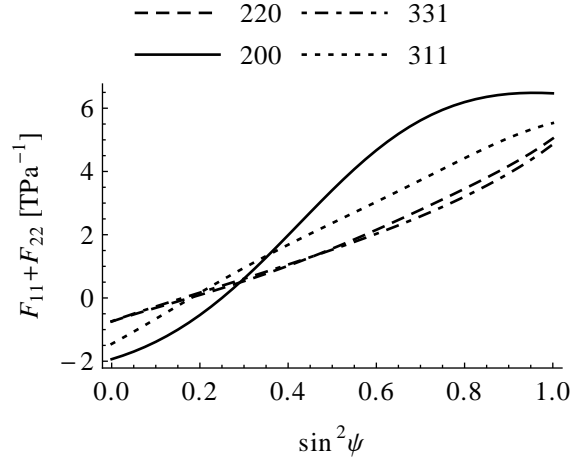


Figure 2.4: Untextured Ni, Vook-Witt stress factors  $F_{11} + F_{22}$  versus  $\sin^2 \psi$  ( $\phi = 0$ ).

The constitutive equation in matrix form reads

$$\begin{pmatrix} \varepsilon_{11}^S \\ \varepsilon_{22}^S \\ \varepsilon_{\perp}^S \\ 0 \\ 0 \\ \varepsilon_{12}^S \end{pmatrix} = \begin{pmatrix} S_{1111} & S_{1122} & S_{1133} & 2S_{1123} & 2S_{1113} & 2S_{1112} \\ S_{1122} & S_{2222} & S_{2233} & 2S_{2223} & 2S_{2213} & 2S_{2212} \\ S_{1133} & S_{2233} & S_{3333} & 2S_{3323} & 2S_{3313} & 2S_{3312} \\ 2S_{1123} & 2S_{2223} & 2S_{3323} & 4S_{2323} & 4S_{2313} & 4S_{2312} \\ 2S_{1113} & 2S_{2213} & 2S_{3313} & 4S_{2313} & 4S_{1313} & 4S_{1312} \\ 2S_{1112} & 2S_{2212} & 2S_{3312} & 4S_{2312} & 4S_{1312} & 4S_{1212} \end{pmatrix} \begin{pmatrix} \sigma_{\parallel}^S \\ \sigma_{\parallel}^S \\ \sigma_{33}^S \\ \sigma_{23}^S \\ \sigma_{13}^S \\ 0 \end{pmatrix} \quad (2.34)$$

We proceed as in the Vook-Witt solution, expressing all unknowns as a function of a single constant (in this case, we choose  $\sigma_{\parallel}^S$ ). Ruling out the 1<sup>st</sup>, 2<sup>nd</sup> and 6<sup>th</sup> row from Equation 2.34 and separating unknown terms, we obtain:

$$\begin{pmatrix} \varepsilon_{\perp}^S \\ 0 \\ 0 \end{pmatrix} - \sigma_{\parallel}^S \begin{pmatrix} S_{1133} + S_{2233} \\ 2S_{1123} + 2S_{2223} \\ 2S_{1113} + 2S_{2213} \end{pmatrix} = \begin{pmatrix} S_{3333} & 2S_{3323} & 2S_{3313} \\ 2S_{3323} & 4S_{2323} & 4S_{2313} \\ 2S_{3313} & 4S_{2313} & 4S_{1313} \end{pmatrix} \begin{pmatrix} \sigma_{33}^S \\ \sigma_{23}^S \\ \sigma_{13}^S \end{pmatrix} \quad (2.35)$$

Equation 2.35 can then be solved for  $(\sigma_{13}^S, \sigma_{23}^S, \sigma_{33}^S)$  as a function of  $\varepsilon_{\perp}^S$  and  $\sigma_{\parallel}^S$ . Now, substituting this result back into the 3<sup>rd</sup> row of equation 2.34, we obtain a



2.1. Grain interaction modelling for X-ray diffraction stress measurements

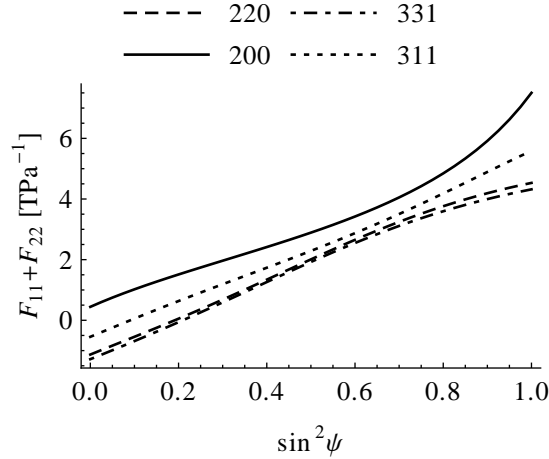


Figure 2.5: Untextured Ni, inverse Vook-Witt stress factors  $F_{11} + F_{22}$  versus  $\sin^2 \psi$  ( $\phi = 0$ ).

linear equation that can be solved for  $\varepsilon_{\perp}^S$  in terms of  $S_{ijkl}$  and  $\sigma_{\parallel}^S$  only. Finally,  $(\varepsilon_{11}^S, \varepsilon_{12}^S, \varepsilon_{22}^S)$  can be easily written as a function of  $\sigma_{\parallel}^S$  by expanding rows 1, 2 and 6 in Equation 2.34. As in the Vook-Witt case, the process needs to be repeated for every rotation in the Euler space, since the compliance matrix is rotated.

After all unknowns have been expressed in terms of one single constant, the in-plane stress  $\sigma_{\parallel}^S$ , the latter can be assigned a virtual value and corresponding virtual, bulk average stresses and strains can be evaluated. The bulk average elastic tensor components can then be calculated from the virtual strain to stress ratios. Stress factors are calculated in a similar fashion, not unlikely how it was done in the Vook-Witt approach: once bulk average, virtual stress and strain components are collected, the ODF-weighted average diffraction strain  $\{\varepsilon_{33}^L\}$  is calculated at each  $hkl, \phi, \psi$  and stress factors are returned as in Equation 2.32.

Figure 2.5 shows calculated stress factors  $F_{11} + F_{22}$  for untextured Nickel under the inverse Vook-Witt model.

**Extending Vook-Witt and inverse models to general loading states** Expressions for Vook-Witt and inverse models were expanded considering relatively simple macroscopic strain or stress states, enforcing the (reasonable) in-plane isotropy hy-

pothesis for thin films and coatings. Truly, the definition only states that crystallites are subject to identical, but not necessarily rotationally symmetric, in-plane strain (Vook-Witt) or stress (inverse). In the most general case, Vook-Witt ( $VW$  subscript) and inverse Vook-Witt ( $iVW$  subscript) strain and stress, respectively become [16]

$$\begin{aligned}\varepsilon_{VW} &= \begin{pmatrix} \langle \varepsilon_{11}^S \rangle & \langle \varepsilon_{12}^S \rangle & \varepsilon_{13}^S \\ \langle \varepsilon_{12}^S \rangle & \langle \varepsilon_{22}^S \rangle & \varepsilon_{23}^S \\ \varepsilon_{13}^S & \varepsilon_{23}^S & \varepsilon_{33}^S \end{pmatrix} \\ \sigma_{iVW} &= \begin{pmatrix} \langle \sigma_{11}^S \rangle & \langle \sigma_{12}^S \rangle & \sigma_{13}^S \\ \langle \sigma_{12}^S \rangle & \langle \sigma_{22}^S \rangle & \sigma_{23}^S \\ \sigma_{13}^S & \sigma_{23}^S & \sigma_{33}^S \end{pmatrix}\end{aligned}\quad (2.36)$$

It naturally follows that elastic constants determination for a general loading state becomes more complicated, as additional, virtual strain (stress) components shall enter the algorithm, in different steps. As this is of limited relevance to the polycrystalline thin film elastic constants determination problem, formulas will not be expanded.

### 2.1.1.3 Modelling experimental data

Grain interaction models introduced so far return elastic constant from extremal strain or strain distribution hypothesis, enforcing all crystallites to display identical stresses or strain along given directions. Hill proved that, in bulk materials, Reuss and Voigt hypotheses constitute the lower and upper bound, respectively, for elastic moduli [9]. The same idea can, in fact, be extended to direction-dependent models: the Vook-Witt and its inverse approach, despite their complex formulation, only enforce either hypothesis (constant strain or stress) in a direction-dependent fashion. It is therefore not unreasonable to assume that a Hill weighted average approach can take different, direction-dependent weights [13, 6]. The Reuss, Voigt, Vook-Witt and inverse models then constitute the boundaries within which a real material's behaviour is expected to be found.

For a given stress problem, a set of experimental points are collected, usually at different sample  $\psi$  tilts and  $\phi$  rotations, and often for different  $hkl$  reflections. It is common practice to collect a reasonably high number of experimental points, in order to improve statistics. A least squares minimisation is then performed, according to

### 2.1. Grain interaction modelling for X-ray diffraction stress measurements

Equation 2.10, in order to obtain the stress components  $\langle \sigma_{kl}^S \rangle$  after measured strains  $\{\varepsilon_{33}^L\}$  and calculated X-ray elastic stress factors  $F_{ij}$ . When a combination of models is involved, one can indicate with  $m_k$  the material volume fraction obeying the  $k$ -th model assumptions;  $\sum_k m_k = 1$  and  $0 \leq m_k \leq 1$  need to be enforced to ensure physical meaning to the solution. Equation 2.10 thus becomes

$$\{\varepsilon_{33}^L\} = \sum_k m_k F_{ij}^{(k)} \langle \sigma_{kl}^S \rangle$$

where  $F_{ij}^{(k)}$  indicate the stress factors calculates as per the  $k$ -th model. Unless specific assumptions are being enforced (such as  $m_1 = m_2 = 0.5$  for arithmetic averaging), volume fraction parameters  $m_k$  add to the total of minimisation parameters in the least squares algorithm.

An example is shown in Figure 2.6. Experimental data was kindly provided by U. Welzel [13], modelling was performed using the QXrdTex software package using four grain interaction models (Reuss, Voigt, Vook-Witt and inverse) and assuming an equibiaxial stress state. The least squares algorithm returns an in-plane residual stress value of  $162MPa$ ; linear combination coefficients 0.41 (Reuss), 0.00 (Voigt), 0.42 (Vook-Witt) and 0.17 (inverse Vook-Witt). As a comparison,[13] reports a  $165MPa$  residual stress value; linear combination coefficients 0.3, 0.0, 0.6 and 0.1 respectively.

#### 2.1.2 Morphological texture

So far only crystallographic texture was discussed. Preferred orientation however can show up in terms of grains having aligned, elongated shapes, without necessarily having a connection with preferred orientation in crystalline domains. Modelling morphological texture usually makes use of the Eshelby-Kröner description, which is hereby described.

**Eshelby-Kröner** The Eshelby-Kröner elastic grain interaction model, originally devised for studying the effect of an inclusion in a polycrystalline matrix, was revised for the study of a polycrystalline aggregate whose grains display elongated shapes [17]; each grain is treated as an inclusion in the polycrystalline matrix, and the final elastic tensor is calculated iteratively.

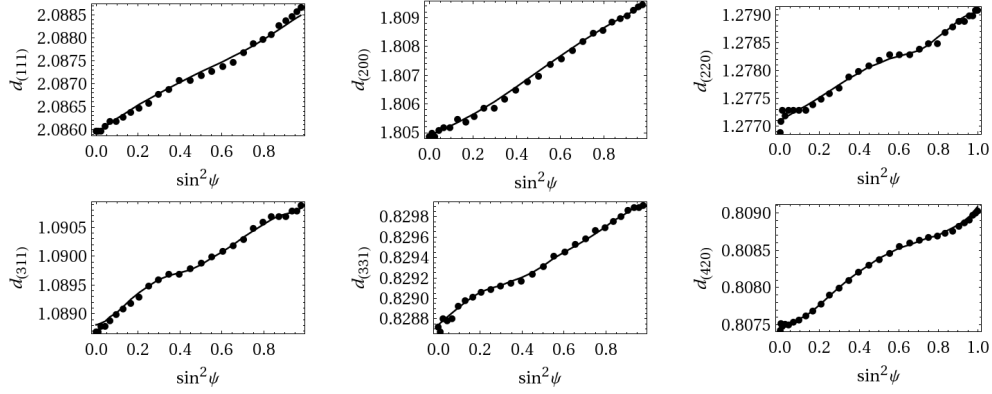


Figure 2.6: Sputtered Cu thin film  $d_{hkl}$  versus  $\sin^2 \psi$  plots for six  $hkl$  families. Black dots show experimental points, modelling is shown as a continuous line. Data courtesy of U. Welzel [13].

Following the procedure found in literature, the stress and strain in a single grain can be written as

$$\sigma = p \langle \sigma \rangle \quad \text{and} \quad \varepsilon = q \langle \varepsilon \rangle \quad (2.37)$$

with  $p$  and  $q$  being suitable fourth-rank tensors, depending on the grain principal axes rotation in respect to the aggregate (Euler  $\alpha, \beta, \gamma$ ); so that

$$p = C q \langle C \rangle \quad \text{and} \quad q = S p \langle S \rangle \quad (2.38)$$

The effect of an inclusion can be separated as

$$\begin{aligned} p &= \langle C \rangle + r \\ q &= \langle S \rangle + t \end{aligned} \quad (2.39)$$

The Euler space average of  $r$  and  $t$  is zero, because

$$\begin{aligned} \langle \sigma \rangle &= \langle C + r \rangle \langle \varepsilon \rangle = \langle C \rangle \langle \varepsilon \rangle \Rightarrow \langle r \rangle = 0 \\ \langle \varepsilon \rangle &= \langle S + t \rangle \langle \sigma \rangle = \langle S \rangle \langle \sigma \rangle \Rightarrow \langle t \rangle = 0 \end{aligned} \quad (2.40)$$

### 2.1. Grain interaction modelling for X-ray diffraction stress measurements

For the sake of convenience,  $r$  and  $t$  can be written as

$$r = \langle C \rangle v \quad \text{and} \quad t = u \langle S \rangle \quad (2.41)$$

Let us now assume that a single grain does not fit into the matrix. Ideally, one can imagine that a strain free shape has been cut out, deformed plastically up to  $\varepsilon_P$  and then put back into the matrix, with which it interacts elastically. Some relaxation will occur at the interface, resulting in a final strain,  $\varepsilon_G$  in the grain. The stress will then be  $\sigma = C(\varepsilon_G - \varepsilon_P)$ , but also  $\varepsilon_G$  will be proportional to the permanent deformation withstood by the grain, that is

$$\varepsilon_G = \omega^{-1} \varepsilon_P \quad (2.42)$$

where  $\omega$  is called Eshelby tensor. If an external strain,  $\langle \varepsilon \rangle$ , is applied, the local stress can be written as

$$\begin{aligned} \sigma &= (\langle C \rangle - \langle C \rangle \omega) \varepsilon_G + \langle C \rangle \langle \varepsilon \rangle \\ \sigma &= C(\varepsilon_G + \langle \varepsilon \rangle) \end{aligned} \quad (2.43)$$

so that

$$\begin{aligned} \varepsilon &= -(C - \langle C \rangle + \langle C \rangle \omega)^{-1} (C - \langle C \rangle) \langle \varepsilon \rangle \\ u &= -(C - \langle C \rangle + \langle C \rangle \omega)^{-1} (C - \langle C \rangle) \\ v &= (\omega - I)(-u) \end{aligned} \quad (2.44)$$

An expression for the Eshelby tensor is now needed. If we define  $E = \omega^{-1} \langle S \rangle$ , we can take the result from [18], and implement it in our procedure:

$$E_{ijkl} = \frac{a_1 a_2 a_3}{8\pi} \int_0^\pi \sin \psi d\psi \int_0^{2\pi} d\phi \frac{D_{ik}^{-1} k_j k_l + D_{jl}^{-1} k_i k_k}{\left[ (a_1 k_1)^2 + (a_2 k_2)^2 + (a_3 k_3)^2 \right]^{\frac{3}{2}}}$$

where  $\mathbf{a}$  contains the length of the principal axes of an ellipsoidal inclusion (often expressed in term of aspect ratios  $\eta_1 = a_1/a_3$  and  $\eta_2 = a_2/a_3$ );  $\mathbf{k}$  is the position vector with components  $(\sin \psi \cos \phi, \sin \psi \sin \phi, \cos \psi)$ ; and  $D_{ij} = \langle C_{ijkl} \rangle k_k k_l$ .

The algorithm starts with a guess for  $\langle S \rangle$  (for instance, one may take the corresponding

isotropic polycrystal's compliance) and proceeds scaling the  $\omega$  tensor iteratively, until the condition  $\langle u \rangle = \langle v \rangle = 0$  is met. For this purpose, it is convenient to use the scalar averages  $\tilde{u} = \sum_{ijkl} u_{ijkl}^2$  and  $\tilde{v} = \sum_{ijkl} v_{ijkl}^2$ , and set a threshold value for them after which the iteration process will be stopped. At the end of iterations, the method returns the correct  $\omega$  and  $\langle S \rangle$ . It is worth to note that the Eshelby-Kröner grain interaction model is self-consistent, i.e. produces the same results whether calculations are performed in terms of stiffness or compliance.

The X-ray stress factors calculation is rather straightforward once  $\omega$  and  $\langle C \rangle = \langle S \rangle^{-1}$  are available, and involves averaging the  $u$  tensor over the diffracting crystallites only, combining Equations 2.44, 2.41, 2.39 and 2.37.

Example stress factors are shown for polycrystalline, texture-free Nickel, with different grain aspect ratios in Figures 2.7 and 2.8.

**Baczmanski** An alternative grain interaction model for free-surface conditions was recently proposed by [19]. Following a similar approach to that of Vook and Witt for crystallographic texture, Baczmanski et al. suggest enforcing the Eshelby-Kröner model in-plane, and the Reuss model in the out-of-plane direction. From a practical point of view, the tensor  $p$  in Equation 2.37 is rewritten as  $p^B$ , as follows

$$p_{ijkl}^B = \begin{cases} I_{ijkl} & i = 3 \text{ or } j = 3 \\ p_{ijkl} & i \neq 3 \text{ or } j \neq 3 \end{cases} \quad (2.45)$$

Bulk and XRD elastic constants calculation follows the same procedure as in the Eshelby-Kröner model, once the correction from Equation 2.45 is applied.

### 2.1.2.1 Modelling experimental data

Fitting experimental data with morphological texture grain interaction model involves finding the optimal grain aspect ratio, that yields the lowest (weighted) sum of residuals. Since the calculation of elastic constants is computationally expensive, the best approach consists in performing a least squares regression using stress factors calculated with a given aspect ratio; the (weighted) sum of squared residuals is then plotted against the aspect ratio, in order to find a minimum. Since most thin films possess

2.1. Grain interaction modelling for X-ray diffraction stress measurements

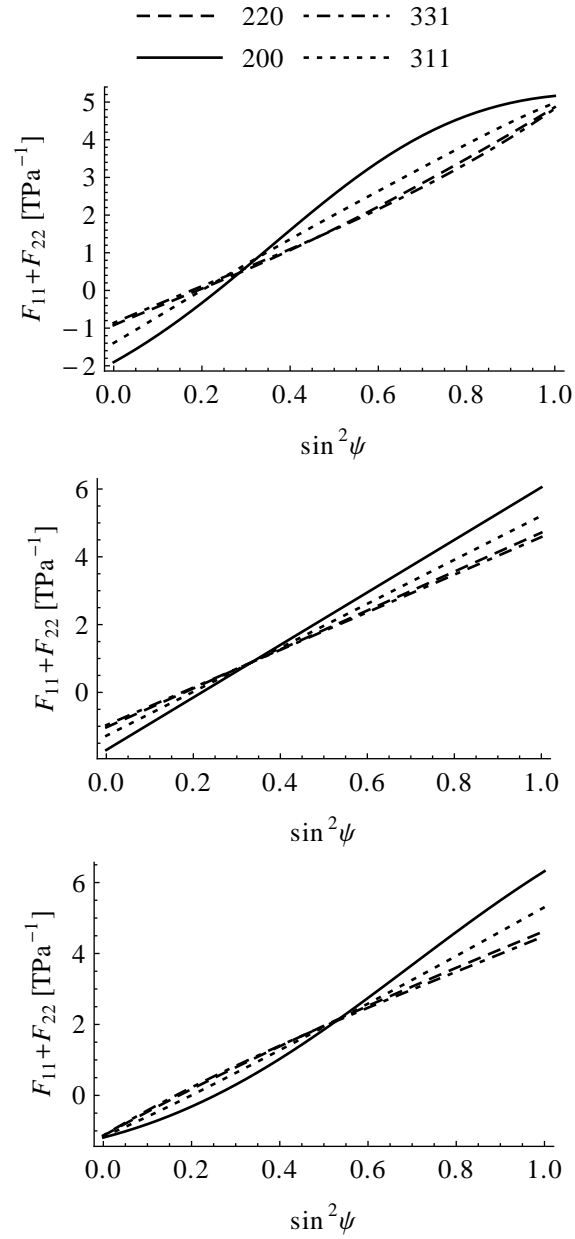


Figure 2.7: Eshelby-Kröner stress factors ( $F_{11} + F_{22}$ ) as a function of  $\sin^2 \psi$ , for different grain aspect ratios: from the top left, clockwise,  $\eta_1 = \eta_2 = 0.1, 1, 10$ .

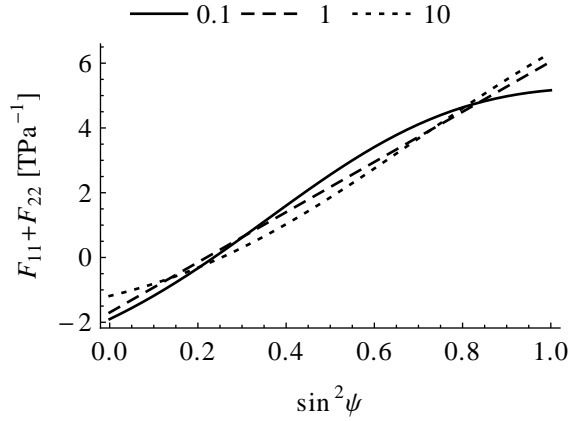


Figure 2.8: Eshelby-Kröner stress factors ( $F_{11} + F_{22}$ ), comparison between different aspect ratios for peak 200.

two equivalent directions (the in-plane axes  $x_1^S$  and  $x_2^S$ ), it is physically reasonable to assume that grains assume an elongated (or flat) shape, with identical aspect ratio along the two minor axes, i.e.  $\eta_1 = \eta_2$ , hence reducing significantly the number of solutions to explore.

An example is shown in Figure 2.9. Modelling is performed, using the Eshelby-Kröner grain interaction model, on the same data set as in Figure 2.6, data were kindly provided by U. Welzel [13]. The minimisation returned a residual stress value of 156 MPa, the best fitting grain aspect ratio being 0.85 (slightly elongated grains). The fit with the Eshelby-Kröner model is visibly not as good as with using crystallographic texture models; the resulting residual stress value is however almost the same.

## 2.2 The QXrdTex software package

Modelling grain interaction is, computationally speaking, no easy task. Moreover, there is no readily available software package that can provide reliable algorithms for the calculation of X-ray elastic constants (or stress factors) from texture data and use them in fitting experimental curves. For these reasons, a new software was developed [20], to perform X-ray diffraction stress data analysis by applying the grain interaction



## 2.2. The QXrdTex software package

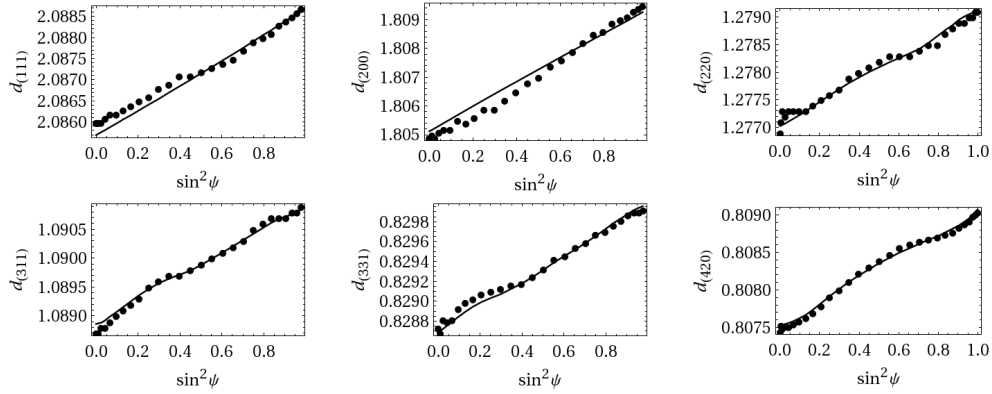


Figure 2.9: Fitting X-ray diffraction strain data with the Eshelby grain interaction model. Sputtered Cu from [13].

models described in Chapter 2.1.

**Design principles** The need for a software package for XRD stress analysis of a textured components arises from the fact that algorithms are computationally expensive. Implementation in computer algebra or numerical computation systems is not very effective in terms of performance, hence the requirement for a high performance environment such as a compiled language. As lots of procedures imply the use of trial and error, the software was designed with extensibility and programmability in mind. Finally, only portable and open-source libraries were used to ensure availability to about any target system.

The program was divided in three layers: an engine providing a set of highly optimised algorithms, JavaScript bindings for the engine functions and a user interface offering a script editor and an array of tools to ease the programming task, including a wizard to help the user automatically set up the most common analysis tasks.

**Implementation** The software package was programmed using C++, linking to the GNU Scientific Library [21] for numerical functions, and the Qt libraries [22] for the scripting interpreter (Qt Script module) and the user interface (Qt Gui module). As a first step, Qt-based wrapper classes for all used GSL objects were implemented, to ensure results such as lists or matrices to be easily accessible from the scripting

## Chapter 2. Stress and texture relationships in films by means of XRD

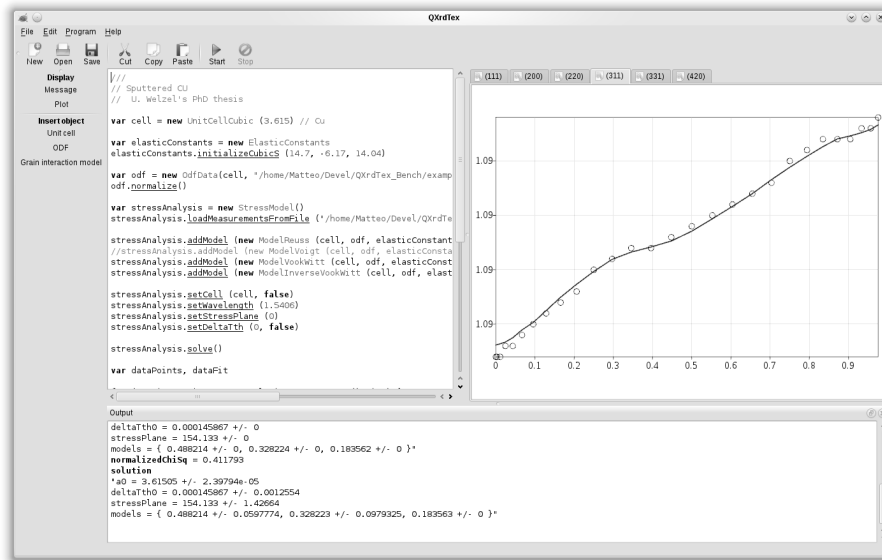


Figure 2.10: The QXrdTex software main window.

engine. Subsequently, new custom types such as an elastic tensor or ODF class were introduced.

Eventually, the XRD stress and texture elaboration algorithms were implemented, by making use of custom classes only, so that every piece of code would be able to be exposed by the user-controlled scripting engine. Objects and methods for simulation and data analysis were finally linked using Qt Script bindings to the JavaScript interpreter.

The user interface was designed as a single-instance text editor for the script code, featuring several programming aids, such as code snippets and a wizard to automate the most common analysis tasks. A custom plot package was implemented and linked to the engine, in order to provide charting capabilities. Finally, the script engine was implemented to run on a separate thread, to ensure interface responsiveness during calculations, and also allowing emergency stops.

## 2.3 Measuring elastic grain interaction

Elastic grain interaction models can take different forms, based on a wide array of assumptions. Hypotheses however refer to extremal cases, deemed the upper or lower bound of a true material's behaviour (see e.g. the reasoning underlying Hill averaging [9]); effectively, grain interaction models rely on assumptions that do not necessarily hold true for any case study. On top of this, calculating elastic constants requires accurate knowledge of several microstructural parameters, such as the single crystal elastic constants, as well as the orientation distribution function; the latter especially is rather problematic when morphological effects are to be taken into account. On the other hand, in some cases measuring the actual elastic constants for a thin film is of special interest for the final component application, especially when mechanical reliability is a key factor.

Stress state in thin films is most often expected to be simple. In-plane directions are equivalent thanks to symmetry arguments, so in-plane stress components are equal

$$\sigma_{11}^S = \sigma_{22}^S = \sigma_{\parallel} \quad (2.46)$$

and hence  $\sigma_{12}^S = 0$ . Moreover, as the surface is expected to be homogeneous, at least within a reasonable area,

$$\frac{\partial \sigma_{ij}^S}{\partial x_1^S} = \frac{\partial \sigma_{ij}^S}{\partial x_2^S} = 0 \quad (2.47)$$

As the surface is stress-free (i.e.  $\sigma_{13}^S = \sigma_{23}^S = \sigma_{33}^S$ ), one can enforce the divergence theorem ( $\partial \sigma_{ij} / \partial x_j = 0$ ) to obtain

$$\begin{aligned} \frac{\partial \sigma_{11}^S}{\partial x_1^S} + \frac{\partial \sigma_{12}^S}{\partial x_2^S} + \frac{\partial \sigma_{13}^S}{\partial x_3^S} &= 0 \Rightarrow \sigma_{13}^S = 0 \\ \frac{\partial \sigma_{21}^S}{\partial x_1^S} + \frac{\partial \sigma_{22}^S}{\partial x_2^S} + \frac{\partial \sigma_{23}^S}{\partial x_3^S} &= 0 \Rightarrow \sigma_{23}^S = 0 \\ \frac{\partial \sigma_{31}^S}{\partial x_1^S} + \frac{\partial \sigma_{32}^S}{\partial x_2^S} + \frac{\partial \sigma_{33}^S}{\partial x_3^S} &= 0 \Rightarrow \sigma_{33}^S = 0 \end{aligned} \quad (2.48)$$

In the end, it is reasonable to assume that only the  $\sigma_{\parallel}$  component is to be found in a thin film.

**The Stoney formula** These considerations led Stoney [23] to formulate a simple equation to calculate the stress state in a film based on substrate curvature. Provided a film is deposited on a substrate with initial curvature  $1/R_0$ , should a residual stress state arise during film deposition, the final component will show a curvature of  $1/R$  with  $R \neq R_0$ . Given the film thickness  $t_f$ , the substrate thickness  $t_s$  and the substrate's Young modulus in the bending direction  $E_s$ , we can enforce equilibrium as follows

$$\begin{aligned}\sigma_{\parallel} t_f + \int_0^{t_f} E_s \frac{x_3^S}{R} dx_3^S &= 0 \\ \int_0^{t_f} E_s \frac{(x_3^S)^2}{R} dx_3^S &= 0\end{aligned}\quad (2.49)$$

yielding

$$\sigma_{\parallel} = \frac{E_s t_s^2}{6 t_f} \left( \frac{1}{R} - \frac{1}{R_0} \right) \quad (2.50)$$

The Stoney formula has one strong limitation. While the thickness of the substrate can be measured with good relative accuracy, and the substrate Young's modulus obtained by a simple bending test, the result is very sensitive to film thickness and sample curvature, whose evaluation is not always an easy task. However, provided the measurement can be conducted reliably, the Stoney residual stress value can prove a handy reference point.

**Rocking curve of monocrystalline substrates by XRD** The residual stress value given by the Equation 2.50 relies heavily on an accurate measurement of substrate curvature. This problem can be addressed in an elegant and effective way on monocrystalline substrates, such as Silicon wafers for electronic applications.

As shown in Figure 2.11, when a single crystal is bent, its atomic planes parallel to the surface are rotated by an  $\omega$  angle which is a function of the position along the sample. The corresponding diffraction peak will then be found at the same  $2\theta$  Bragg angle, but only after tilting the sample holder by an angle  $\omega$ ; if said  $\omega$  peak position is acquired in at least two points along the sample surface, curvature can be easily measured as pointed out in [24].

$$\frac{1}{R} = \frac{\partial \omega}{\partial x_1^S}$$

### 2.3. Measuring elastic grain interaction

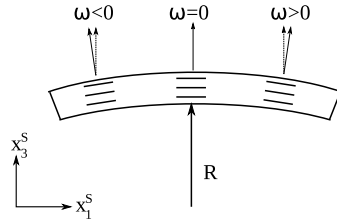


Figure 2.11:  $\omega$  diffraction peak shift in bent single crystal.

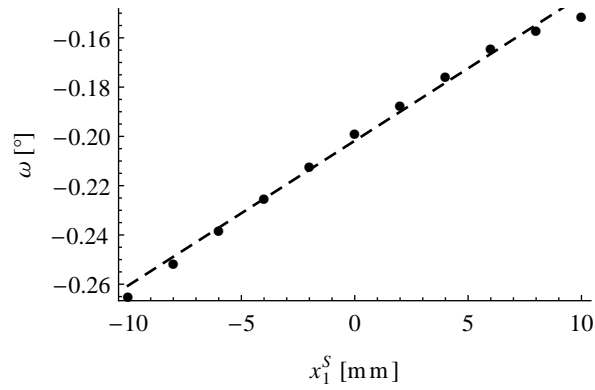


Figure 2.12: Rocking curve of monocrystalline ( $h00$ ) Si after deposition of a Tungsten film.

An example application is shown in Figure 2.12. The rocking curve was measured on a ( $h00$ ) Silicon wafer upon which a film of pure Tungsten was deposited by means of magnetron sputtering. The measured radius of curvature is  $(170.0 \pm 0.2) \text{ mm}$ .

#### 2.3.1 XEC evaluation by curvature methods

As already mentioned, thin film X-ray elastic constants are often difficult to calculate, as they require accurate knowledge of other microstructural parameters which is not always readily available. However, experimental measurement is possible: if the residual stress state is known, for example by relying on the Stoney formula, X-ray elastic constants can be evaluated as the strain to stress ratio.

We have already seen in Section 2.1 that for an untextured polycrystal we have (Equation 2.16)

$$\{\varepsilon_{33}^L\} = \left( 2S_1(hkl) + \frac{1}{2}S_2(hkl) \sin^2 \psi \right) \sigma_{\parallel} \quad (2.51)$$

so that  $(1/2)S_2(hkl)$  can be calculated as the slope of the linear fit of  $\{\varepsilon^L\}$  versus  $\sin^2 \psi$ , divided by the in-plane stress  $\sigma_{\parallel}$  [25]. Similarly,  $2S_1(hkl)$  is calculated from the intercept of said linear regression. Note that  $S(hkl)$  indicates the *effective* elastic moduli for a given  $hkl$  direction, and not the single-crystal moduli; see also Section 2.1 for a more detailed description.

If the sample can be assumed to be intrinsically isotropic, the  $hkl$  dependence wanes from  $S$ , so that the macroscopic elastic moduli can be immediately calculated. Else, one may recall [10] that the macroscopic elastic strain corresponds to that measured on a reflection with  $3\Gamma = 0.6$ ; if X-ray elastic constants measured along several  $hkl$  directions are plotted against  $3\Gamma$ , the equivalent macroscopic compliance in terms of  $\langle S_1 \rangle$  and  $\langle 1/2S_2 \rangle$  can be obtained by interpolation.

If the sample cannot be assumed to be texture-free, then X-ray stress factors  $F_{ij}$  introduced in Equation 2.10 can be evaluated as the  $\{\varepsilon_{33}^L\}$  to  $\sigma_{\parallel}$  ratio [25] as

$$\begin{aligned} \{\varepsilon_{33}^L\} &= F_{ij} \sigma_{ij}^S = (F_{11} + F_{22}) \sigma_{\parallel} \\ \Rightarrow (F_{11} + F_{22}) &= \frac{\{\varepsilon_{33}^L\}}{\sigma_{\parallel}} \end{aligned} \quad (2.52)$$

This way, the  $F_{11} + F_{22}$  sum can be assessed by performing XRD strain measurement at any  $(hkl, \phi, \psi)$  which is the object of interest.

An example application is hereby shown. An  $1\mu m$  thick Tungsten film was deposited by means of magnetron sputtering on a monocrystalline  $(h00)$  Silicon substrate, whose curvature after deposition was measured by collecting the monocrystal's rocking curve by XRD (see also Figure 2.12). In-plane, residual stress value was calculated with the Stoney formula, yielding  $(800 \pm 24) MPa$ . Stress factors are plotted against  $\sin^2 \psi$  in Figure 2.13.

This method however presents two major limitations: 1) it only allows calculating the sum of  $F_{11} + F_{22}$  and 2) it does not allow measuring the macroscopic elastic moduli of the film. Moreover, the procedure is relatively sensitive to accurate knowledge of

### 2.3. Measuring elastic grain interaction

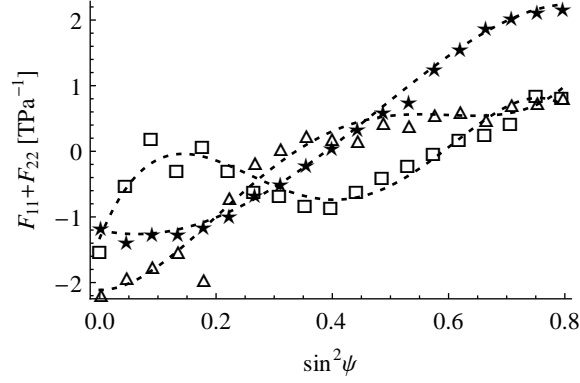


Figure 2.13: Tungsten on monocrystalline Silicon, X-ray stress factors  $F_{11} + F_{22}$  as a function of  $\sin^2 \psi$ . Reflections: 110 ( $\triangle$ ), 200 ( $\square$ ) and 211 ( $\star$ ). Polynomial interpolation shown as dotted line as a guide for the eye.

unit cell parameters: the strain measured by diffraction is

$$\{\varepsilon_{33}^L\} = \frac{\{d\}}{d_0} - 1 \quad (2.53)$$

thus

$$\Delta \{\varepsilon_{33}^L\} = \Delta \left( \frac{1}{d_0} \right) = \frac{1}{d_0^2} \Delta d_0 \quad (2.54)$$

The error on experimental stress factors due to unit cell parameter uncertainty is then

$$\Delta (F_{11} + F_{22}) = \left( \frac{\Delta d_0}{d_0^2} \right) \frac{\{d\}}{\sigma_{\parallel}} \quad (2.55)$$

As will be illustrated in the following paragraphs, higher precision can be achieved by performing in-situ mechanical testing.

#### 2.3.2 In-situ mechanical testing for XEC evaluation

In-situ mechanical testing introduces a further degree of freedom in elastic constants evaluation. This not only allows improving statistics, thus reducing numerical errors, during the calculation; but also permits isolating different terms in the equation, that can hence be evaluated independently. The following procedure constitutes the core

method of analysis developed in the present Thesis work, and has been published in [26].

Let us assume a known load  $\sigma_{11}^A$  is applied along the  $x_1^S$  direction of an untextured sample. X-ray diffraction strain 2.15 then becomes

$$\begin{aligned} \{\varepsilon_{33}^L\} &= \left( S_1(hkl) + \frac{1}{2} S_2(hkl) \sin^2 \psi \cos^2 \phi \right) (\sigma_{\parallel} + \sigma_{11}^A) \\ &+ \left( S_1(hkl) + \frac{1}{2} S_2(hkl) \sin^2 \psi \sin^2 \phi \right) \sigma_{\parallel} \end{aligned} \quad (2.56)$$

This technique allows elastic constants  $S_1(hkl)$  and  $1/2 S_2(hkl)$  to be calculated as  $\partial \{\varepsilon_{33}^L\} / \partial \sigma_{11}^A$ , for  $\phi = 0^\circ$  and  $\phi = 90^\circ$  respectively, hence relying on a different parameter and reducing numerical errors, as explained below. Again, the condition  $S(hkl) = \langle S \rangle$  when  $\Gamma(hkl) = 0.2$  holds true for the calculation of macroscopic compliance.

Where a textured sample is the object of the study, the constitutive equation (2.10) becomes

$$\{\varepsilon_{33}^L\} = F_{11} (\sigma_{\parallel} + \sigma_{11}^A) + F_{22} \sigma_{\parallel} \quad (2.57)$$

Expanding the stress factors expression (Equation 2.9), we obtain

$$\begin{aligned} F_{11}(\phi = 0^\circ) &= F_{22}(\phi = 90^\circ) = (A_{3333} - A_{3311}) \sin^2 \psi \\ &\quad - 2A_{3313} \cos \psi \sin \psi + A_{3311} \\ F_{22}(\phi = 0^\circ) &= F_{11}(\phi = 90^\circ) = A_{3322} \end{aligned} \quad (2.58)$$

Eventually,

$$\begin{aligned} \{\varepsilon_{33}^L\}(\phi = 90^\circ) &= (\sigma_{\parallel} + \sigma_{11}^A) F_{11}(\phi = 90^\circ) + \sigma_{\parallel} F_{22}(\phi = 90^\circ) \\ &= (\sigma_{\parallel} + \sigma_{11}^A) F_{22}(\phi = 0^\circ) + \sigma_{\parallel} F_{11}(\phi = 0^\circ) \end{aligned} \quad (2.59)$$

hence both  $F_{11}$  and  $F_{22}$  can be calculated in terms of  $\partial \{\varepsilon_{33}^L\} / \partial \sigma_{11}^A$ , by performing two separate measurements at  $\phi = 0^\circ$  and  $\phi = 90^\circ$ ; in other words, repeating the measurement at  $\phi = 90^\circ$  is equivalent to applying a load along  $x_2^S$  while measuring at  $\phi = 0^\circ$ .



### 2.3. Measuring elastic grain interaction

In-situ mechanical testing offers two major advantages. First, it is quite immediate to realize that individual stress factors  $F_{ij}$  rather than the sum  $F_{11} + F_{22}$  can be measured independently. Second, the technique is arguably less sensitive to accurate knowledge of unit cell parameters. We have

$$\Delta F_{ij} = \Delta \left( \frac{\partial \{\varepsilon_{33}^L\}}{\partial \sigma_{ij}^A} \right) = \frac{2(\Delta d_0)^2}{d_0^3} \frac{\partial \{d\}}{\partial \sigma_{ij}^A} \quad (2.60)$$

so that the impact of the error induced by uncertainty on the  $d_0$  unstrained planar spacing (hence unit cell parameters) is reduced from  $\Delta d_0/d_0^2$  to  $2(\Delta d_0)^2/d_0^3$ .

It is important to add that the result from Equation 2.59 should be taken into account to further reduce experimental error; by exploiting this, the number of experimental points per unknown is at least doubled, allowing a reduced error. For any given  $(hkl, \psi)$ , data points can be arranged as  $(\sigma_{11}^A, 0, \{\varepsilon_{33}^L\})$  when  $\phi = 0^\circ$ , and  $(0, \sigma_{11}^A, \{\varepsilon_{33}^L\})$  when  $\phi = 90^\circ$ , remembering how  $F_{11}(\phi = 0^\circ) = F_{22}(\phi = 90^\circ)$  and vice versa. This way a linear regression with two independent variables can be performed, modelling together data points collected at different  $\phi$  values for the same  $hkl$  and  $\psi$ ; moreover, the resulting constant term is but  $\sigma_{\parallel}$ , which can be compared to the same result obtained from Stoney's formula.

**In-situ four-point bending** While an uniaxial tensile test would seem easier from a theoretical point of view, it poses strict requirements on sample preparation and geometry; because of the need of clamping, an uniaxial tensile test cannot be performed on brittle substrates; finally, there is no easy way to measure the actual stress applied to the film. For these reasons, although the technique has seen applications [27], other methods are usually preferred.

Four-point bending instead presents several advantages. The substrate can be a simple rectangular slab (opportunately cut to size), which is easy to manufacture; additionally, supports do not stress the substrate significantly. The main advantage of four-point bending, however, is the possibility of carefully evaluating the applied stress by means of curvature measurements. In four-point bending, the bending moment, and therefore the sample curvature radius, are constant in the central section. Therefore,

assuming bending occurs around the  $x_2^S$  axis, the stress on its surface will be

$$\sigma_{11}^S = \frac{E t}{R 2} \quad (2.61)$$

where  $E$  is the elastic modulus along the  $x_1^S$  direction,  $R$  is the beam curvature radius and  $t$  the beam thickness. Now, if the sample is a thin film deposited on top of a substrate, the thickness becomes  $t_s$  (reasonably assuming  $t_f \ll t_s$ ), while the Young modulus to be applied is  $E_f$ , the effective average elastic modulus of the film along the  $x_1^S$  direction. The latter parameter is initially unknown; it can however be calculated, along with the other results, by following a two-step procedure.

First, an initial guess for the in-plane elastic modulus  $E_f'$  is provided; this can be calculated using a grain interaction model such as those described in Section 2.1, or, more simply, by taking the Young modulus of the corresponding bulk material (the guess doesn't need to be precise). First-iteration X-ray elastic constants  $A'_{33kl}$  (or stress factors  $F'_{ij}$ ) are then calculated, as well as a first guess of the residual in-plane stress value,  $\sigma'_{\parallel}$ . Finally, the in-plane residual stress result from Stoney's formula is enforced, leading to scaling the just calculated X-ray elastic constants, along with the in-plane elastic modulus  $E_f$ , by a factor of  $\sigma'_{\parallel}/\sigma_{\parallel}^{(Stoney)}$ .

Four-point bending has the further advantage of allowing reduced experimental error on the residual stress value given by Stoney's formula. A four-point bending device is likely to support a loading cell, yielding the measured load applied on the sample. As long as the actual to nominal load is a linear function (which is a reasonable expectation), one can extrapolate the zero-load curvature from curvature measurements at each loading step. As this method increases the number of points used in evaluation, statistical error is expected to decrease.

The technique is not flawless: first, the applied stress is not homogeneous, but a slight gradient unfolds across the film's thickness; this effect is however negligible, if we consider that the substrate is usually at least three orders of magnitude thicker. Second, the anticlassic deformation of the bar is constrained by clamping; this is however not relevant when a secondary, independent applied stress measurement is conducted by other means, such as curvature measurement. Third, Poisson coefficient mismatch between film and substrate may lead to the rise of a small stress component in the  $x_2^S$  direction [27]; this is however negligible in most cases, due to being a few

### 2.3. Measuring elastic grain interaction

percent of the applied load along the main direction. Lastly, and more importantly, the technique is harder to apply on multi-phase objects, because load is distributed in an unknown fashion among constituents; in this case, new hypotheses or conditions need to be found and enforced.

Despite the aforementioned issues, the procedure can be applied to a large number of case studies; in the end, it returns the residual stress in the film (calculated by the Stoney formula and confirmed with X-ray diffraction); the X-ray elastic constants; and the in-plane, bulk elastic modulus of the coating.

#### 2.3.3 Effects of texture gradients

It is not uncommon for relatively thick ( $\mu m$ ) coatings to display a gradient of either stress or texture along the direction perpendicular to the surface. This is due to substrate interface effects being confined to the very few material layers, within a thickness that varies as a function of several parameters. Under these premises, any material property discussed so far (stress, texture, stress factors) need to be expressed no longer as an absolute quantity, but as a function of a spatial coordinate; namely, the  $x_3^S$  direction, normal to the sample surface.

Gradient characterisation can be effectively performed by means of diffraction, by exploiting radiation absorption by the sample material. Absorption changes significantly as a function of the beam incidence angle on the sample surface, to the point that gauge volumes for different  $hkl$  reflections can be quite different. More importantly, absorption is a function of radiation wavelength: if a measurement is repeated under different photon energies, results may differ under the presence of a gradient, and need to be related to the average *information depth*[28] involved.

Different photon energies may be obtained by using different radiation tubes, e.g. repeating a measurement under Cu and Cr radiations; eventually, however, the choice is limited. Better possibilities are offered by employing synchrotron radiation, because wavelength can be tuned arbitrarily within a given emission range. This is especially useful because it allows repeating a measurement close to the absorption edge of the sample main element(s); under these conditions in fact, absorption may change by up to two orders of magnitude within few electronvolts. The advantage is given by the likeness of instrumental conditions: instrumental corrections in fact are not expected

to change significantly under such a low energy shift; immediate comparison of results is therefore possible [29].

Experimental data points need to be associated to their corresponding information depth  $\overline{x_3^S}$ , defined as

$$\overline{x_3^S} = \frac{\int_0^t x_3^S \exp(-x_3^S/\xi) dx_3^S}{\int_0^t \exp(-x_3^S/\xi) dx_3^S}$$

where  $t$  is the layer thickness and  $\xi = \sin \theta \cos \psi / (2\mu)$ ;  $\mu$  is the target material's linear absorption coefficient, and is a function of wavelength. The value that is actually measured for a generic property  $P$  is similarly written as

$$\overline{P} = \frac{\int_0^t P(x_3^S) \exp(-x_3^S/\xi) dx_3^S}{\int_0^t \exp(-x_3^S/\xi) dx_3^S}$$

Eventually, property  $P$  as a function of depth within the material layer  $x_3^S$  can be obtained by interpolation; for most applications, and due to the fact that repeating a measurement is expensive in terms of machine time, a linear interpolation is assumed to suffice.

## Chapter 3

# Methods and Materials

This Chapter briefly illustrates instrumental setups and measurement techniques employed in experiments presented in this Thesis work. A quick introduction on X-ray diffraction equipment is initially offered; following, an extensive introduction to electrodeposited coatings is presented.

### 3.1 Methods: X-ray diffraction analysis

X-ray diffraction measurements were equally performed with conventional laboratory instruments and synchrotron radiation. Features of both instrumental setups are here briefly presented.

**Panalytical X’Pert MRD** The diffractometer is originally designed for stress and texture characterisation, and is equipped with a four-circle goniometer. A pseudo-parallel beam is obtained with a polycapillary lens, which allows reaching  $0.3^\circ$  divergence in the incident beam. This configuration provides reasonable specimen illumination in unfavourable conditions (such as low  $2\theta$  or high  $\psi$ ), while also ensuring a sufficiently large specimen area to be invested by the beam in any configuration, allowing for good grain statistics [30].

A vertical slit collimator (divergence  $0.27^\circ$ ) and a graphite flat-crystal analyser are installed before the detector.

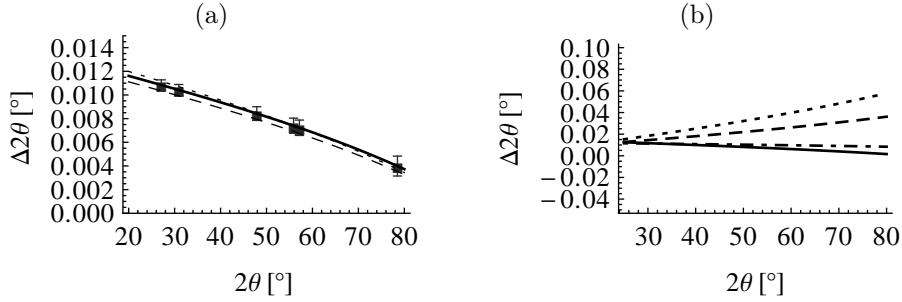


Figure 3.1: Instrumental  $2\theta$  correction for the MCX beamline goniometer. (a)  $9.4\text{keV}$ , at  $\psi = 0^\circ$  (solid line),  $\psi = 70^\circ$  (dotted line) and  $\psi = -70^\circ$  (dashed line); square dots mark the ZnO peak positions used for characterization. (b)  $\psi = 0^\circ$ , photon energy  $7\text{keV}$  (solid line),  $9.4\text{keV}$  (dot-dashed line),  $15\text{keV}$  (dashed line) and  $18\text{keV}$  (dotted line).

**The MCX beamline** The MCX beamline at Elettra Synchrotron in Trieste was used for several experiments, whose results are presented in this thesis. The beamline was designed to provide a highly versatile setup for materials characterisation purposes, from crystalline powders to heavily worked surfaces, to highly anisotropic objects such as films and fibres.

Optics consist of a tangentially collimating mirror, a double-crystal monochromator which also provides sagittal focusing, and a second, tangentially refocusing mirror. The first element consists of a Platinum coated,  $1.2\text{m}$  long flat Silicon crystal, with a surface roughness of less than  $3\text{\AA}$ . This crystal is mounted on a bending mechanism with a root mean square residual tangential slope of less than  $5''$ .

Full characterisation of instrumental corrections for flat plate samples was conducted by analysing high resolution data collected from standard samples [31]. A mixture of NIST SRM 640a (pure Silicon) [32] was blended with commercial, pure ZnO powder, and a high resolution pattern was collected in order to obtain accurate values for the ZnO powder unit cell parameters; pure ZnO was then used in assessing instrumental  $2\theta$  corrections at several energies and sample tilt angles. Silicon SRM instead was not employed, because the standard powder grains are too coarse, and result in poor statistics when installed in flat plate geometry. Instrumental  $2\theta$  corrections are shown in Figure 3.1.

### 3.1. Methods: X-ray diffraction analysis

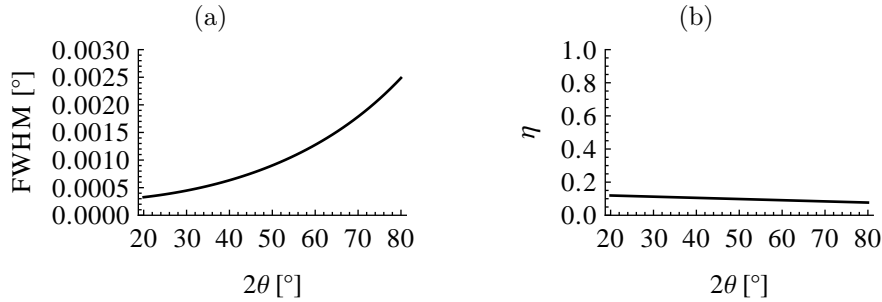


Figure 3.2: MCX instrumental peak shape at 15 keV: full width at half maximum (a) and pseudo-Voigt  $\eta$  (b).

The NIST SRM 660a (Lanthanum Hexaboride) [33] was used to characterise instrumental peak shape. The Caglioti [34] function parameters (full width at half maximum, and pseudo-Voigt  $\eta$  mixing parameter) for  $15\text{keV}$  and  $\psi = 0^\circ$  are reported in Equation 3.1. Corresponding plots are shown in Figure 3.2.

$$\begin{aligned} FWHM [^\circ] &= 3.419 \times 10^{-3} \tan^2 \theta - 2.130 \times 10^{-4} \tan \theta + 2.586 \times 10^{-4} \\ \eta &= 1.336 \times 10^{-1} - 7.117 \times 10^{-4} \theta [^\circ] \end{aligned} \quad (3.1)$$

#### 3.1.1 Four-point bending device for in-situ mechanical testing

In recent years [35], a four-point bending device for in-situ testing, named SCRX-01, was designed and built, for installation on the Panalytical X'Pert MRD diffractometer. During the course of the present work, an adaptor was also realised for installation of the device on the MCX goniometer cradle [31]. The device is shown in Figure 3.3.

Testing samples should be ideally  $8 \times 80\text{mm}$  in size ( $\pm 2\text{mm}$ ), and between 0.5 and 2mm in thickness. Outer blades are located 70mm apart, inner ones 40mm. Load may vary between  $-30$  and  $+30\text{N}$ , and an internal extensometer provides an accurate reading of the actual load. Accurate calibration of the device is required to produce reliable X-ray strain results.

First, as XRD strain measurements require several hours (at least, with conventional laboratory radiation sources), stability over time is mandatory. For this purpose, a

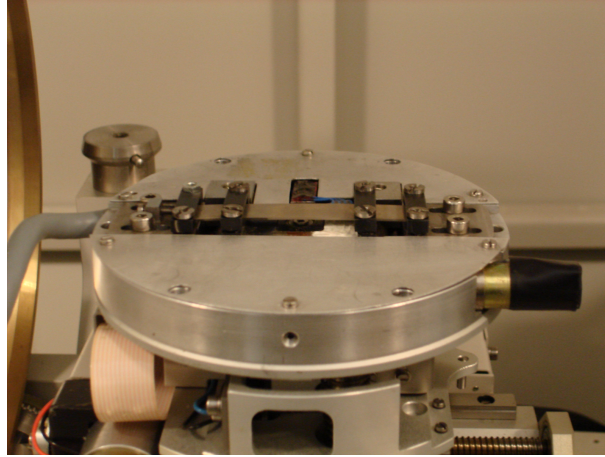


Figure 3.3: The SCRX-01 four-point bending device installed on the Panalytical X'Pert MRD diffractometer.

monocrystalline  $h00$  Silicon substrate was installed on the device, and bent under a load of  $5N$ . Curvature was measured by means of diffraction peak  $\omega$  shift, over a course of  $16h$ ; as seen in Figure 3.4, no peak shift is visible, confirming the device stability over the course of long measurements.

The X-ray elastic constants measurement requires actual applied load to be evaluated carefully. For this purpose, it is important to verify that the actual response to imposed nominal load follows a known, possibly linear calibration. Again, monocrystalline  $h00$  Silicon was used for characterisation, as the actually applied load can be very accurately measured by means of curvature measurements, performed in a non-contact fashion by means of diffraction. Figure 3.5 shows that the response of the cell is linear, as required for proper experimental applications.

## 3.2 Materials: electrodeposited coatings

Electrodeposition is common in coating applications, thanks to the technique's low cost and easy implementation. The process involves the application of an electric potential to promote reduction of metallic ions from a bath, at the surface of a metallic substrate, in order for a deposit to grow on top of the latter. These deposits are mainly



3.2. Materials: electrodeposited coatings

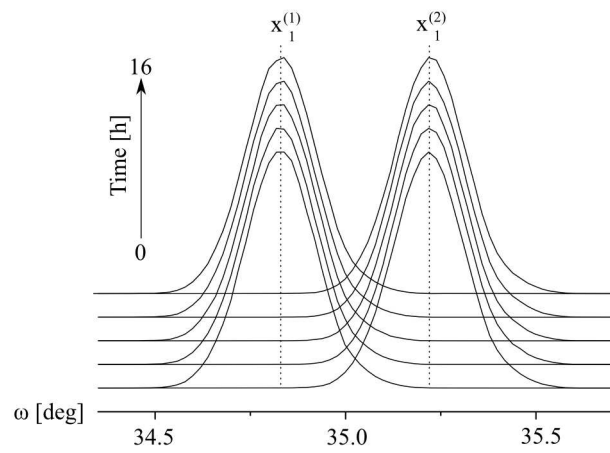


Figure 3.4: Bending device stability over time, Si(400)  $\omega$  peak position in two different positions along the  $x_1^S$  axis, over the course of 16h.

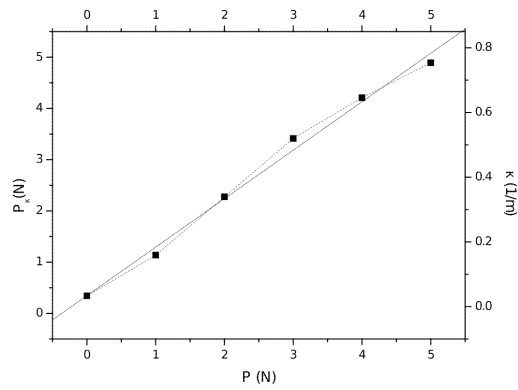


Figure 3.5: SCR-X-01 measured actual load versus nominal load. Calibration performed with monocrystalline  $h00$  Silicon.

employed for corrosion and wear protection applications, but in special cases they have been employed also to alter the surface magnetic, thermal and optical characteristics [36].

Electrodeposition mainly produces polycrystalline films [37]. Growth at the substrate interface often shows pseudomorphism, a term that indicates the continuation of grain boundaries and other microstructural features from the substrate into the deposit, without crystalline continuity as defined for epitaxial growth. The latter epitaxial growth is also possible, provided that the substrate is carefully polished and pickled; that deposition material crystalline structure is similar to the substrate's; and that energetically favourable crystalline planes are exposed by the substrate.

Structure-zone diagrams are drawn in terms of bath temperature and current density; e.g., high temperature and low current promotes the formation of columnar structures with large grains, whereas low temperatures and high current densities produce acicular-shaped, fine grains, thanks to the increased nucleation rate. Structure-zone description can be enriched by also taking bath additives into account; in fact, several types of chemicals are added to the solution, to regulate pH, act as surfactant and thus promote gas bubble removal from the growing film, and more. Finally, the current regime may be pulsed to promote microstrain relaxation during the “off” phase, while maintaining a high nucleation rate during the “peak” phase to obtain a fine, yet relatively unstrained structure.

Since a few decades ago [38], interest has arisen in the field of technological applications of electrocodeposition, a process referring to the embedding a secondary phase (usually solid particles from the electrolytic bath) in the electrodeposit. Such particles have an impact on the crystallisation process, leading to microstructural changes.

With these premises, electrodeposited coatings make an ideal candidate for studying residual stress and texture relationships in films. Deposition mechanisms and conditions are briefly discussed.

### **3.2.1 The electrodeposition process**

The electrodeposition process occurs when an electric potential is applied to a conductive substrate immersed in a bath containing metallic ions, so that a reduction reaction occurs at the substrate surface, leading to formation of a metallic deposit.

### 3.2. Materials: electrodeposited coatings

This process, albeit simple in theory, is governed by a very large amount of parameters [37], such as substrate geometry and surface preparation; chemicals in the deposition bath, such as acids or bases employed in pH regulation, surfactants to avoid gas bubble inglobation (and consequent embrittlement); and perhaps most importantly, the electrical potential and subsequent current density.

Current pulsation was found to positively affect the deposition process [39, 40], allowing a higher current density to be employed. Higher current density in fact means higher nucleation rate, but also higher tensile microstrains, which ultimately have a negative effect on the final mechanical properties. Pulsation offers a periodic time lapse during which microstrains are allowed to relax; eventually, a finer and less strained microstructure is achieved.

**Effect of sonication** Past works [41] have given attention to the application of ultrasounds in chemical processes, as a method to promote phase dispersion and mixing, affect crystallisation processes and promote gas removal. Power ultrasounds (in the range just above human hearing) have been successfully employed in electrodeposition, with positive effects on the quality of deposits in terms of adhesion, morphology and, most importantly, gas removal [42, 36]. Hydrogen bubbles forming on the cathode surface are promptly removed by ultrasonic waves before they can get trapped in the substrate, reducing pitting issues in the final component and replacing (or adding to the effect of) other kind of surfactant additives commonly employed in gas removal.

**Electrocrystallisation** The grain nucleation and growth process in these deposits is often called *electrocrystallisation*. Most electrodeposits exhibit a structure that is determined by concurrent epitaxial and pseudomorphic phenomena, where pseudomorphism describes the continuation of grain boundaries and other geometric features from the substrate into the film [37]. When a secondary phase is codeposited, nucleation and growth is altered by the effect of surface interactions occurring between the growing matrix material and the embedded particle. In this case, electrocrystallisation mechanisms are not fully understood, and models proposed only work in a narrow range of deposition parameters [36].

Historically, a first model proposed by Guglielmi [38], states that the secondary phase is adsorbed on the substrate phase, and that metallic ions would subsequently form

an ionic cloud around the adsorbed particle before the reduction reaction takes place. Eventually, such model is only characterised by particle concentration and current density. More recently [43, 44], it was suggested that codeposition only occurs when the precipitate phase particles are able to support an adsorbed layer mainly made by metallic ions; when said ions undergo reduction at the substrate interface, the particle is embedded. Other, more complex models have been proposed ever since, covering different deposits and parameters ranges, but so far no model is able to provide a general approach to the problem. Moreover, so far no valid model has been proposed to address the crystallisation mechanics of electrocodeposition that features nano-scale particles, where different mechanisms, such as Brownian motion, come into play [36].

**Residual stress formation** Texture and mechanical properties of an electrodeposited coating depend heavily on the deposition conditions (and hence the electrocrystallisation process) [45, 46]. The most critical condition is achieved with low temperature, which hinders mobility and thus relaxation, and high current density, which promotes a high nucleation rate. As a consequence of this, tensile residual stresses of intrinsic nature are developed, because of defects such as inclusions or voids, stacking faults or grain boundaries. It is important to note that the majority of the effects which promote homogeneous nucleation also compensate residual stress formation mechanisms, as they help offset defect formation, resulting in a defect-poorer microstructure.

In the end, because of both the complexity and the amount of mechanisms involved, it is difficult to predict the residual stress state on the basis of deposition parameter, and no model is available to get an estimate. For this reason, an experimental measurement is usually the only option to resort to for characterisation.

### 3.2.2 Composite Nickel coatings

Codeposition naturally occurs when a solid phase is suspended in a galvanic bath during deposition. The phenomenon is not yet fully understood, to the point that several models have been proposed, but no one is effectively widely accepted [36].

Since the early studies on codeposition [38], Nickel was employed as matrix material

### 3.2. *Materials: electrodeposited coatings*

for a wide array of tests, thanks to its popularity as a coating material, featuring a large variety of materials as codeposited phase. Wide interest has been especially shown for Silicon carbide and alumina embedded particles, which can greatly enhance the coating's wear resistance and hardness, to the point of being able to provide a substitute for hard Chromium [36]. More recently [47, 36] interest has been shown for employing nano-scale particles as precipitate phase in composite coatings. Thanks to the higher surface-to-volume ratio, the effect of the secondary phase on the metallic matrix is maximised, and such the strengthening effect; in particular, special attention was given to Silicon carbide and alumina nanoparticle embedding in polycrystalline Nickel.

The secondary phase is known to affect electrocrystallisation in several ways. In respect to a pure Nickel coating, Silicon carbide nanoparticles precipitation yield a more homogeneous and smooth surface, made up of finer grains, which also show a rounder shape. Alumina precipitates, on the other hand, still positively affects morphology, leaving a more compact and homogeneous structure in respect to pure Nickel. The coating surface is however rougher and grains coarser, when compare to the film featuring Silicon carbide nanoparticles [36].

Crystallographic texture is also heavily influenced by the presence of nanoparticles. It has been reported [48, 49] that the presence of SiC microparticles promotes the rise of 100 and 110 fibre texture poles. This effect is expected to be magnified if the precipitate phase is added in the form of nano-scale particles, because of the higher surface to volume ratio. No significant effect has been reported to be found after addition of an  $\text{Al}_2\text{O}_3$  precipitate phase; the latter in fact is known to agglomerate, thus having a reduced impact on crystalline growth, and owes most of its beneficial effect to precipitation strengthening mechanisms.

*Chapter 3. Methods and Materials*

## Chapter 4

# Stress and texture relationship in nanocomposite galvanic coatings

Electrodeposited coatings display a large amount of different morphologies, crystallisation textures and residual stress states. Hence, they make an ideal case for the study of texture, elastic properties and residual stress relationships. Deposition conditions and nanoparticles embedding effects on the final coating properties are hereby presented.

It is worth to note that the goal of this activity is the application of the elastic properties characterisation method described in the previous Chapters to real cases of technological interest. For this reason, products and working conditions have been chosen on the basis of investigations conducted in previous works (in particular, [36]).

**Electrodeposition parameters** Based on prior works [36] and practice, identical deposition conditions have been used for all samples described in this Chapter. A standard Watt's bath was used, with the following composition:  $240\text{g/l}$   $\text{NiSO}_4$ ,  $45\text{g/l}$   $\text{NiCl}_2$ ,  $30\text{g/l}$   $\text{H}_3\text{BO}_4$ ; moreover,  $0.1\text{g/l}$  sodium dodecylsulphate was added as surfactant, to promote gas bubble removal. Pulsed  $1\text{Hz}$  current with  $2\text{A/dm}^3$  peak intensity

was applied. Temperature was held at  $45^{\circ}\text{C}$  using a thermostat. These conditions promote fast nucleation, thanks to the high peak current density, but also microstrain relaxation during the “off” phase of the pulsed current regime; also, the final coating is especially dense, to the point that residual porosity is negligible.

Deposition time is calculated as a function the required final thickness, on the basis of current density and area to be coated, assuming a perfectly dense layer. the latter assumption is very abstract (does not take into account not only possible inclusions, but also grain boundaries), and area estimates are very approximate. Combining with instrumental errors, the final thickness ends up being within 20-25% of the goal.

**Experimental considerations** All films showed a tensile residual stress state, as expected for coatings deposited under a high density, pulsed current. In-situ mechanical testing was performed under tensile loads on the film: loading is in fact more critical to the substrate rather than the coating, the latter being able to withstand higher stress levels without undergoing plastic deformation [26]. Moreover, applied loads on the film varied on a per-sample basis, the upper limit being about 200 MPa. In order to verify that plastic deformation did not ensue, XRD peak shape was monitored, and verified that it remained constant as applied load was increased. It is in fact known that upon plastic deformation, diffraction peak width increases because of microstrains arising from dislocation formation.

## 4.1 Elastic properties characterisation in a pure Nickel coating

The first characterisation, both in chronological and logical order, was performed on a pure Nickel coating. A  $4\mu\text{m}$  thick film was deposited on a  $0.8\text{mm}$  low-carbon steel sheet; results were used as a demonstration of the residual stress and X-ray elastic constants experimental measurement technique, as described in 2.3, and published in [26].

X-ray diffraction pole figures and stress analysis have been performed on peaks 200, 220, 311 and 331; these peaks have, on average, high intensity, and do not overlap any signal from the substrate. In-situ mechanical testing was performed under 9



4.1. Elastic properties characterisation in a pure Nickel coating

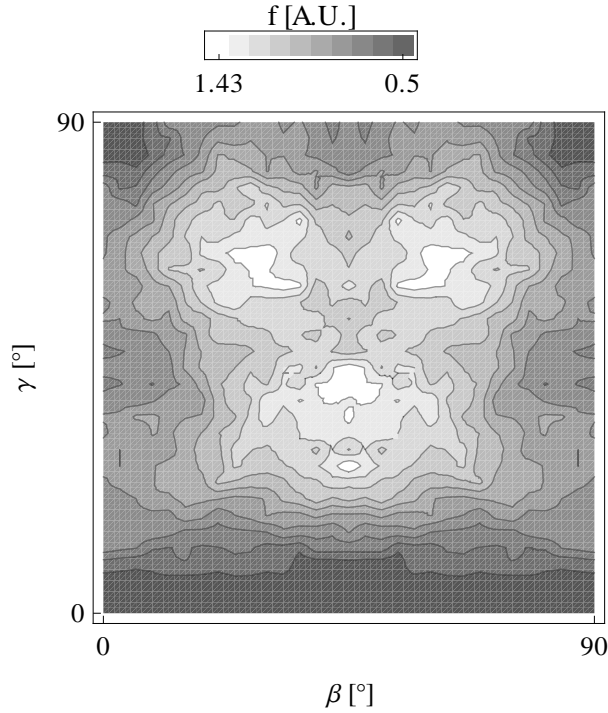


Figure 4.1:  $4\mu\text{m}$  Nickel on steel; ODF section at  $\alpha = 0$ .

loads, from 0 to 16 N on the bending device, corresponding to up to about 200 MPa on the film. The sample presents a relatively soft texture, as seen in Figure 4.1. Residual stress value measured with curvature methods (Section 2.3.2) was found to be  $(440 \pm 20)$  MPa; effective in-plane macroscopic average Young modulus,  $E_f = (182 \pm 13)$  GPa. Experimental stress factors are shown in Figure 4.2.

A comparison with the best-fitting (see Section 2.1.1.3) linear combination of grain interaction models for crystalline texture is offered in Figure 4.3; the best fit is given by  $x_{Reuss} = 0.28$  and  $x_{Voigt} = 0.72$  (both the Vook-Witt and inverse Vook-Witt model account for no contribution). It is immediate to see that calculated stress factors do not reproduce the elastic constants trend as a function of sample tilt. In fact, as illustrated in the following map plot (Figure 4.4), the best-fitting combination of problem parameters likely lies beyond the boundaries of physical meaning; in other words, it is impossible to match experimental values with an average of the extremal

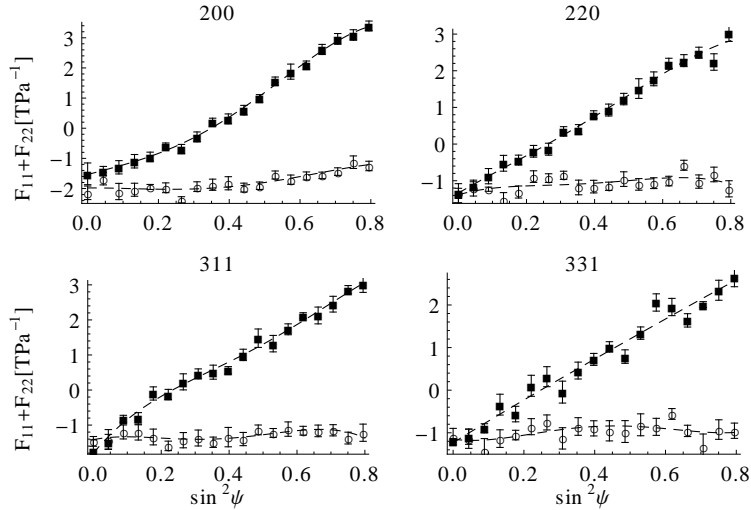


Figure 4.2:  $4\mu\text{m}$  pure Nickel on steel, experimental stress factors  $F_{11}$  (■) and  $F_{22}$  (○). Polynomial interpolation is shown as a dotted line, as a guide for the eye.

grain interaction behaviours.

Similar results are obtained when experimental stress factors are compared with the predictions from morphological texture models (Figure 4.5). The best fitting (see Section 2.1.2.1) grain aspect ratio was found to be 1, corresponding to morphologically isotropic behaviour. This is in contrast with the textured nature of the sample; again, the best fitting solution does not reproduce experimental trends.

Characterisation described in this paragraph was performed as an example of the potential of in-situ mechanical testing for the assessment of elastic properties in a film component. As shown, a good fit of experimental strain data was not possible by means of modelling based on *a priori* assumptions, thus preventing an effective, reliable application of such models to this case. Experimental determination on the other hand has provided accurate results, that do not rely on unverified background hypotheses.

4.1. Elastic properties characterisation in a pure Nickel coating

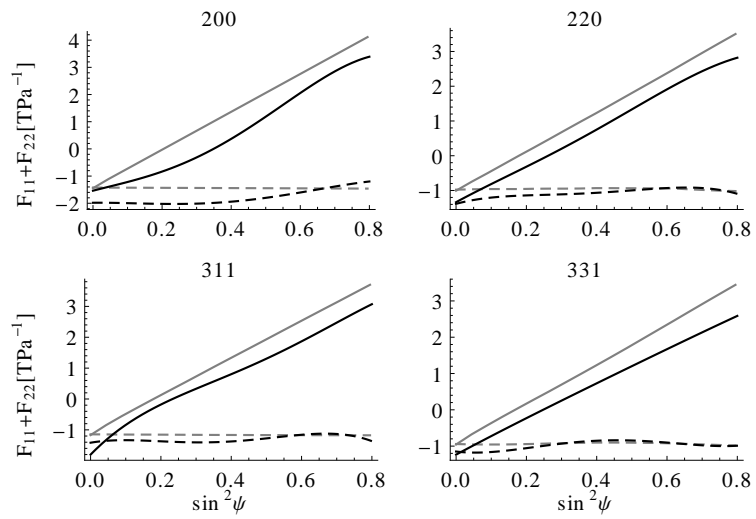


Figure 4.3:  $4\mu\text{m}$  Nickel on steel, experimental stress factors comparison with grain interaction models for crystalline texture. Experimental points interpolation is shown as a black line, modelling as a grey line. A solid line refers to  $F_{11}$ , while a dashed line indicates  $F_{22}$ .

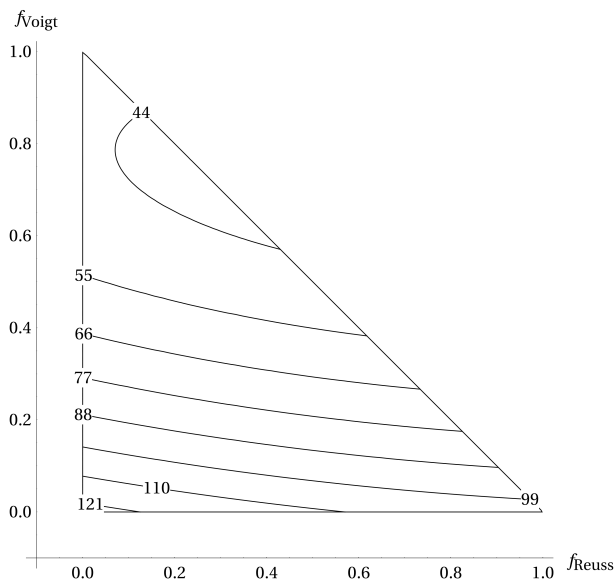


Figure 4.4: Experimental stress factors fit with grain interaction models for crystalline texture. Map of the weighted sum of squared errors as a function of the problem parameters space ( $x_{\text{inverse Vook Witt}} = 0$ ).

4.1. Elastic properties characterisation in a pure Nickel coating

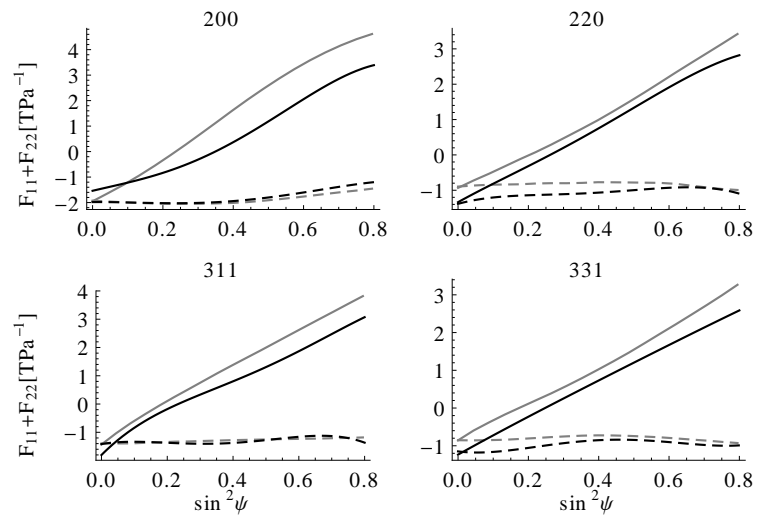


Figure 4.5:  $4\mu\text{m}$  Nickel on steel, experimental stress factors comparison with grain interaction models for morphological texture. Experimental points interpolation is shown as a black line, modelling as a grey line. A solid line refers to  $F_{11}$ , while a dashed line indicates  $F_{22}$ .

## **4.2 Effect of nanoparticle precipitation on texture and residual stress state**

Interest for nanocomposite, Nickel matrix coatings has already been introduced in Section 3.2.2. The codeposition of nanoparticles to galvanic Nickel deposits presents several positive effects on the final mechanic properties, mainly improved hardness and wear resistance [36]. Some recent works [49] have also dealt with characterisation of electrocrystallisation structures under the effect of codeposited particles; however, no accurate study was ever performed on final microstructures influenced by the addition of nanoparticles (as opposed to micrometer-size precipitates), and microstructural effects were not yet related to final, elastic properties. Based on prior works [36], selected Nickel-matrix coatings with different precipitate phases were extensively characterised, both in terms of microstructure (crystallographic texture and morphology) and elastic properties; results are reported in [50].

Three  $20\mu\text{m}$  thick, electrodeposited Nickel matrix nanocomposite coatings have been deposited on low carbon steel plates, cut from the same sheet: one pure Nickel (1), one with addition of SiC nanoparticles (2), and one with  $\text{Al}_2\text{O}_3$  nanoparticles (3).

Silicon carbide nanopowders were produced as the result of the laser pyrolysis of acetylene and silanes by ENEA Frascati; by means of TEM, mean diameter was found to be 20 nm with narrow size distribution; particle shape is spherical and regular. Aluminum oxide was instead purchased by Sigma Aldrich; nanoparticle mean diameter ranges from 5 to 100 nm (with an average of 45); particle shape is still regular and spherical [36]. As previously mentioned, nanoparticle codeposition naturally occurs is the ceramic phase is suspended in the aqueous solution used for electrodeposition. Thickness and distribution of the ceramic powder in the metal matrix was verified by optical microscopy and Transmission Electron Microscopy (TEM) on the polished cross-section of the samples. The volume fraction of embedded nanoparticles, as measured by GDOES analyses, is about 3 ( $\pm 1$ )% for both nanocomposites [36]. Optical micrographs of composite deposits are shown in Figure 4.6, showing visible agglomeration of the alumina phase (darker dots within the light Nickel phase), but good dispersion of Silicon carbide. In fact, no appreciable agglomeration of the SiC codeposit was observed even at lower scale, after TEM observation [50].

Crystalline domain size and shape was measured by X-ray diffraction line profile

#### 4.2. Effect of nanoparticle precipitation on texture and residual stress state

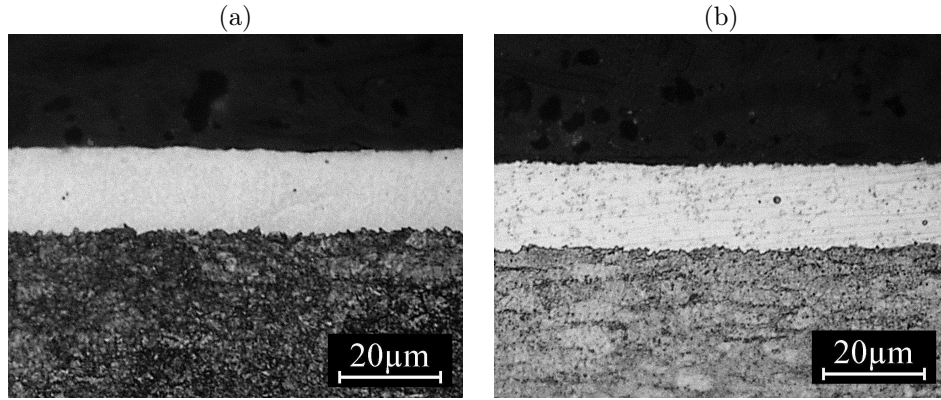


Figure 4.6: Nickel-matrix nanocomposites, with SiC (a) and Al<sub>2</sub>O<sub>3</sub> (b) nanoparticles.

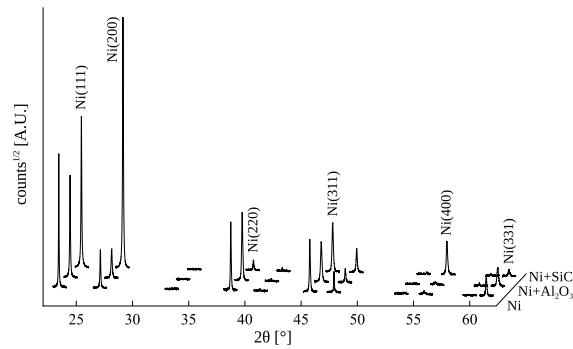


Figure 4.7: Nanocomposite Nickel-matrix coatings, diffraction patterns.

analysis, using the WPPM approach [51] as implemented in the PM2K [52] software package; crystallites were modelled as cylinders, compatible with the elongated shape electrodeposited grains, as often it is assumed. Diffraction patterns are shown in Figure 4.7, and results reported in Table 4.1: it is immediate to appreciate the effect of SiC nanoparticles, which promote the formation of larger, equiaxed domain; whereas no appreciable effect is given by the addition of alumina.

The absence of gradients was verified by means of multiple measurements using differently penetrating X-ray beams; namely, 8.3keV and 8.4keV were selected, these energies being located at either side of Nickel K $\alpha$  absorption edge (8.33keV); as a ref-

Sample	Mean domain size [nm]	Domain aspect ratio
Ni (1)	$61 \pm 28$	0.32
Ni-SiC(2)	$125 \pm 13$	1.05
Ni-Al <sub>2</sub> O <sub>3</sub> (3)	$47 \pm 22$	0.28

Table 4.1: Nanocomposite Nickel-matrix coatings, crystalline domain size and shape.

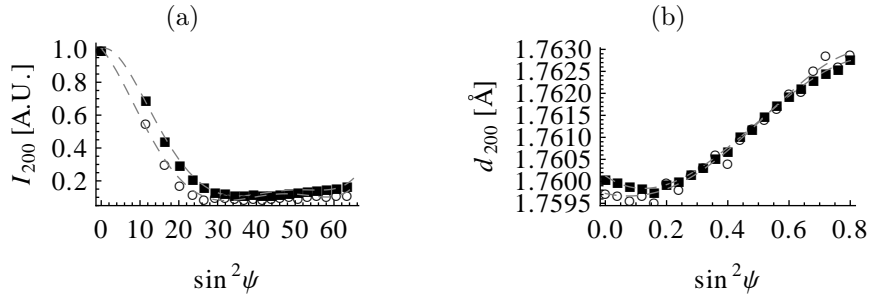


Figure 4.8: Pole figure at  $\phi = 0^\circ$  (a) and interplanar spacing  $d_{200}$  as a function of sample  $\psi$  tilt (b), at 8.3 (■) and 8.4 (○) keV respectively.

erence, consider that average information depth for the 200 peak decreases from about  $2.5\mu\text{m}$  (8.3keV) to about  $1.2\mu\text{m}$  (8.4keV). Figure 4.8 shows an example comparison of the pole figure at  $\phi = 0^\circ$  and measured interplanar spacing  $d_{hkl}$  as a function of  $\psi$  tilt, for the 200 reflection of the sample containing Silicon carbide precipitate phase. No difference is appreciable, therefore the presence of a gradient was excluded.

Collection of pole figures has shown that samples present a fibre texture, as expected; hence, reconstructed pole figures are shown at  $\phi = 0^\circ$  only, in Figure 4.9. Unlike alumina, whose effect isn't noticeable, SiC nanoparticles codeposition affects crystallographic texture as well, promoting the rise of a 100 texture pole (compatibly with observations from [49]).

X-ray stress factors are presented in Figures 4.10, showing  $F_{11}$  and  $F_{22}$  separately, along with a comparison to the best-fitting combination of grain interaction models. A comparison is instead offered in Figure 4.11: the change in crystallographic texture induced by Silicon carbide codeposition reflects in X-ray elastic constants.

As a visual indicator of the goodness of fit, “ $\sin^2 \psi$ ” plots for the Ni+SiC coating are shown in Figure X. The coating is subject to a 177MPa load, hence the split between



#### 4.2. Effect of nanoparticle precipitation on texture and residual stress state

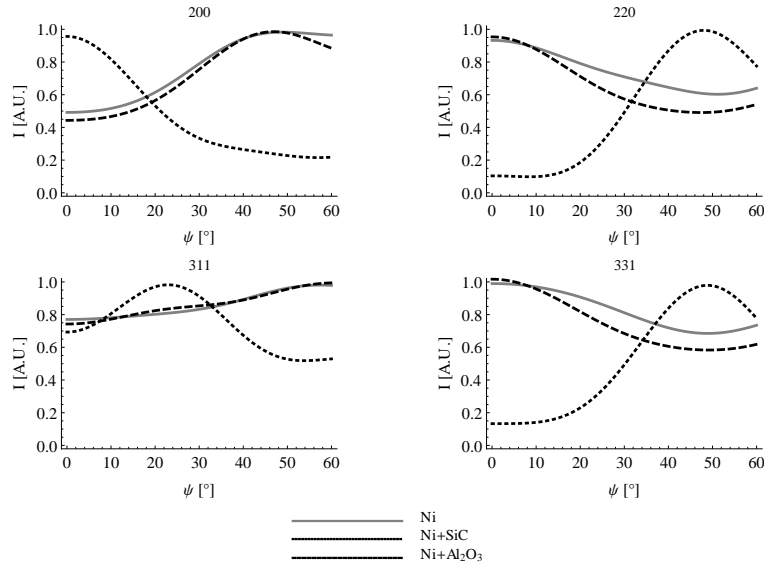


Figure 4.9: Reconstructed pole figures at  $\phi = 0^\circ$ : pure Ni (grey); Ni+SiC (black, dotted); Ni+Al<sub>2</sub>O<sub>3</sub>(black, dashed).

Sample	pure Ni (1)	Ni+SiC (2)	Ni+Al <sub>2</sub> O <sub>3</sub> (3)
$\sigma_{\parallel}^{(Stoney)}$ [MPa]	146 ± 46	207 ± 30	243 ± 32
$E_f$ [GPa]	194 ± 30	203 ± 33	213 ± 16

Table 4.2: Residual stress values and effective in-plane Young modulus.

$\phi = 0^\circ$  and  $\phi = 90^\circ$  directions.

Residual stress and effective, in-plane Young modulus for the studied coatings are found in Table 4.2. In-plane residual stress are of tensile, intrinsic nature as expected for high current densities [45, 46]; stress increases with nanoparticle precipitation, and the effect is larger for alumina than Silicon carbide. In-plane elastic moduli are also affected, and increases observed are in line with what expected from the rule of mixtures for the addition of a stiffer phase (namely, 2 to 3 GPa for 3% SiC, 4 to 6 for Al<sub>2</sub>O<sub>3</sub>).

Nanoparticle addition was shown to significantly affect the electrocrystallisation process [50]. The effect is remarkable for the addition of Silicon carbide, which promotes the formation of larger and equiaxed domains, as well as the rise of a new, sharper

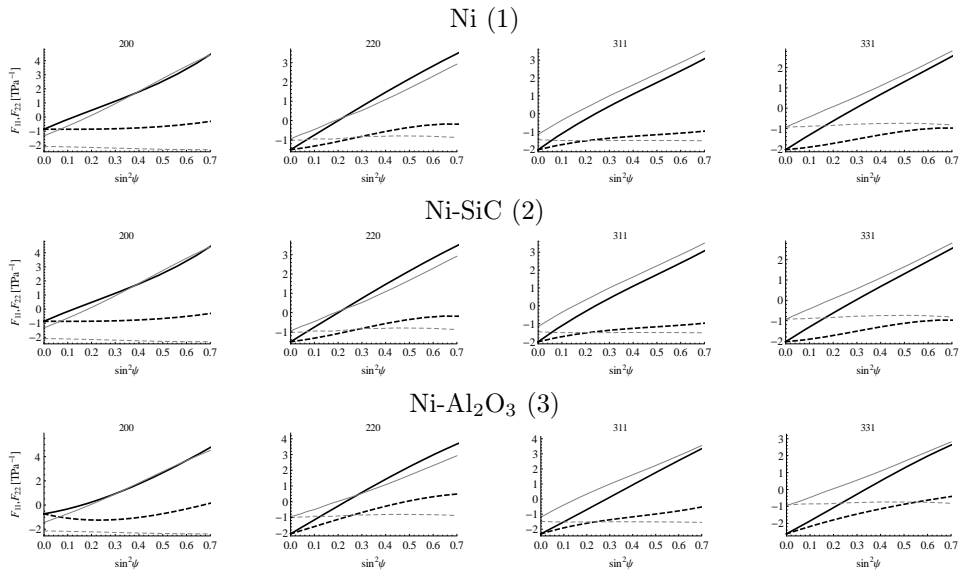


Figure 4.10: Nanocomposite Nickel-matrix coatings, X-ray stress factors  $F_{11}$  (solid line) and  $F_{22}$  (dashed line); experimental (black) versus best-fitting grain interaction models combination (grey).

4.2. Effect of nanoparticle precipitation on texture and residual stress state

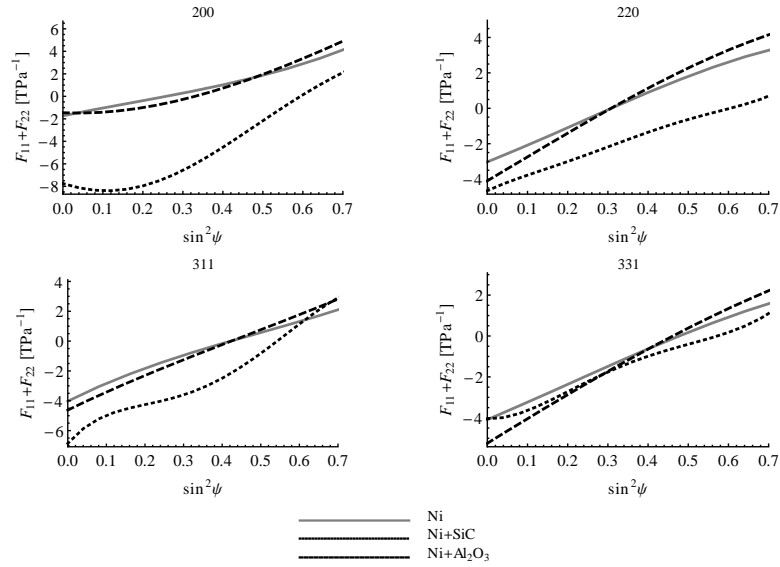


Figure 4.11: Stress factors comparison. Gray lines indicate sample 1 (pure Ni, no nanoparticles), black dashed lines sample 2 (SiC nanoparticles) and black dashed lines sample 3 ( $\text{Al}_2\text{O}_3$  nanoparticles).

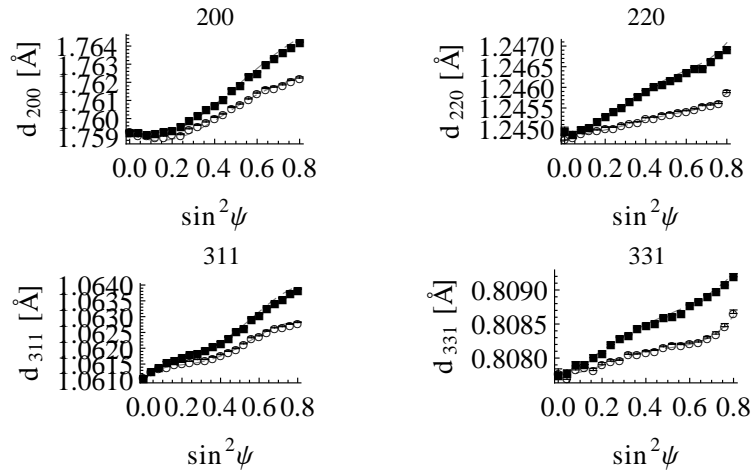


Figure 4.12: “ $\sin^2 \psi$ ” plots for the Ni+SiC coating under a  $177\text{MPa}$  load; directions  $\phi = 0^\circ$  (■) and  $\phi = 90^\circ$  (○). Fit with experimental stress factors shown as dashed, grey line.

Coating thickness [ $\mu m$ ]	$E_f$ [GPa]	$\sigma_{  }$ [MPa]
5.6	$176 \pm 11$	$275 \pm 26$
27.0	$178 \pm 31$	$135 \pm 14$

Table 4.3: Nickel on brass, in-plane residual stress and effective Young modulus.

crystallographic texture pole; this change reflects in the X-ray elastic constants, which display an entirely different trend as a function of  $\psi$  tilt compared to pure Nickel. Alumina codeposition instead has a limited effect on the final product, because of agglomeration, and is only responsible for a slight precipitation hardening effect.

### 4.3 Stress and texture gradients in electrodeposited Nickel on brass

Electrodeposited pure Nickel coatings of different thickness were deposited on brass, following the same procedure and deposition conditions employed in previous cases. Brass was selected as a substrate thanks to its better affinity for Nickel (compared to ferritic steel), in order to maximise surface interactions; for this reason, development of a stress gradient was likely expected as final thickness rises significantly. Two coatings, whose final thickness was measured to be 5.6 and 27.0  $\mu m$  respectively were deposited; residual stress evaluation by curvature (Stoney) methods immediately revealed that a stress gradient is, in fact, present (see Table 4.3), as  $\sigma_{||}$  drops with increasing coating thickness.

X-ray diffraction experiments were performed on reflections 111, 200, 220 and 331, chosen in a way that they do not overlap peaks from the substrate. Initially, residual and X-ray elastic constants were measured using Cu  $K\alpha$  radiation, which has a relatively high penetration depth, so that it returns a reasonable whole-thickness average for the thinner coating. Results are shown in Figure 4.13, and differences between coatings of different thickness are immediately appreciable.

As an indicator of the goodness of fit, a few selected “ $\sin^2 \psi$ ” plots are shown in Figure X, displaying data from both coatings and different reflections, under a 120MPa load. Due to the fact that coatings of different thickness, but deposited under identical conditions, show different elastic properties and residual stress state, further meas-

### 4.3. Stress and texture gradients in electrodeposited Nickel on brass

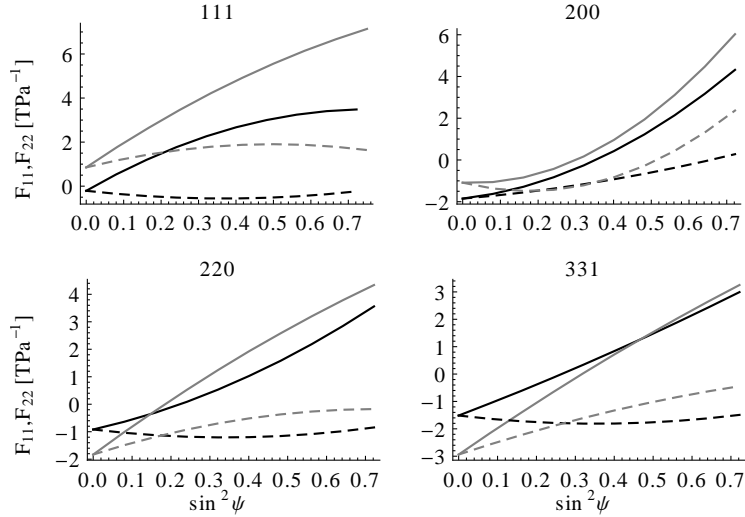


Figure 4.13: Experimental X-ray stress factors, polynomial interpolation; showing  $F_{11}$  (solid line) and  $F_{22}$  (dashed line) for the 5.6 (black) and 27.0 (grey)  $\mu\text{m}$  thick Nickel coatings on brass.

measurements were conducted using synchrotron radiation, on the 5.6  $\mu\text{m}$  coating. Using two different photon energies around Nickel  $K\alpha$  absorption edge, namely 8.3 and 8.4  $\text{keV}$ , average information depth for the 111 reflection is about halved, as shown in Figure 4.15; hence, gradient information can be extrapolated.

The presence of a gradient was in fact assessed within the 5.6  $\mu\text{m}$  coating, as expected. As shown in Figure 4.16, the 111 texture pole becomes sharper as thickness increases. Measured stress also changes slightly, from 275 (whole thickness average) to 258  $\text{MPa}$  (surface layer); the result is in line with expectations. For this latter estimate, an interpolation of stress factors measured for the thin and the thick samples was used.

The presence of a texture gradient requires elastic properties to be characterised by interpolating multiple data sets, collected at different depths within the sample material, e.g. by means of using different photon energies for X-ray diffraction experiments (see Section 2.3.3). Full characterisation was not possible in this case, due to limited synchrotron beamtime availability; therefore, an approximate solution was achieved by interpolating results from a similar sample, deposited under identical conditions, although up to a different final thickness. This approach is not entirely correct from

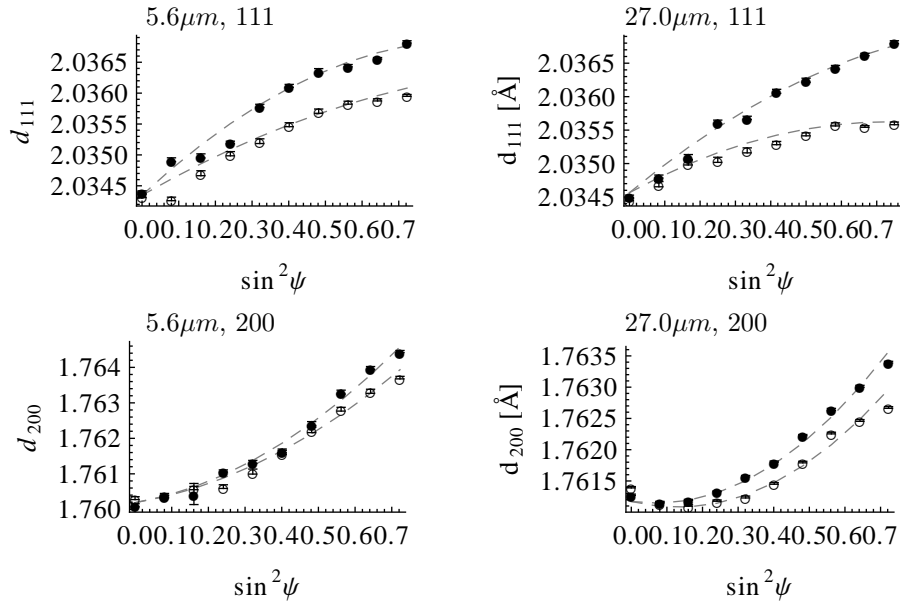


Figure 4.14: “ $\sin^2 \psi$ ” plot for pure Nickel on brass, reflections 111 and 200, thickness 5.6 and  $27.0\mu\text{m}$ ; directions  $\phi = 0^\circ$  (■) and  $\phi = 90^\circ$  (○). Fit with experimental stress factors shown as dashed, grey line.

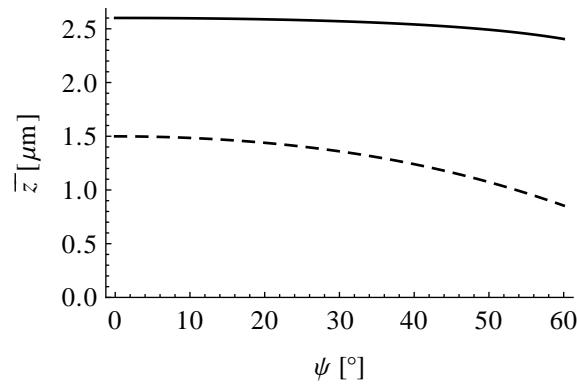


Figure 4.15: Information depth as a function of sample  $\psi$  tilt for Ni 111 peak; 8.3 (solid line) and 8.4keV (dashed line)

4.3. Stress and texture gradients in electrodeposited Nickel on brass

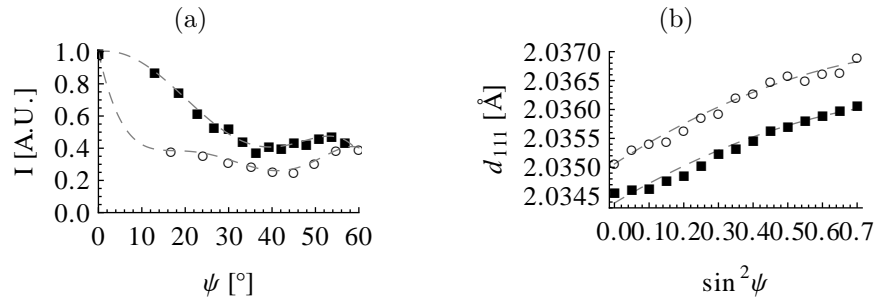


Figure 4.16: Texture and strain gradient in  $5.6\mu\text{m}$  thick Nickel on brass; 111 reflection, pole figures (a) and “ $\sin^2 \psi$ ” plot (b). Whole thickness average ( $8.3\text{keV}$ , black square dots) versus surface layer average ( $8.4\text{keV}$ , empty round dots).

a formal standpoint, because the effect of upper material layers on the bottom ones is *a priori* unknown.; in this particular case a reasonable and consistent solution was provided regardless [29]. It is nonetheless important to remember that such an approximation should be generally avoided, because it potentially leads to wrong conclusions which may not be as glaring in more complex cases, when no comparison to known material is available.

*Chapter 4. Stress and texture relationship in nanocomposite galvanic coatings*



## Concluding remarks

X-ray diffraction stress measurement is a very powerful and reliable technique, often the only solution to the characterisation problem thanks to its unique features. As a possible drawback however, as the technique produces a map of strains, accurate knowledge of the sample material's elastic behaviour is required to calculate residual stresses. When textured samples, such as thin films and coatings, are the object of analysis, the requirement is far from trivial: modelling, based on *a priori* hypotheses, can be applied, but results reliability is not guaranteed.

To address issues discussed above, this Thesis work focuses on a method for experimental characterisation of elastic properties, in terms of X-ray as well as macroscopic elastic constants; the residual stress state is also simultaneously determined. The procedure involves in-situ mechanical testing, which is effectively performed as four-point bending, thanks to several advantages presented by this technique. Gradient effects can also be addressed by means of the same characterisation method, by exploiting the different X-ray beam penetration in the material achieved by adjusting the photon energy.

Elastic properties and residual stress characterisation, by means of X-ray diffraction during in-situ mechanical testing, was employed in characterising several electrodeposited Nickel coatings on different substrates. These samples were chosen because they constitute an ideal case study: the effects of deposition conditions can be carefully investigated. A collection of results was produced, highlighting the microstructural consequences of substrate choice, coating thickness achieved and nanoparticle precipitation.

Extensive and accurate characterisation was possible thanks to the flexibility offered

*Chapter 4. Stress and texture relationship in nanocomposite galvanic coatings*

by experimental procedures. These methods were in fact developed to minimise the need for *a priori* knowledge of microstructural data (especially, single crystal elastic properties), that cannot be easily verified. Moreover, the result is no longer limited by the narrow, and not always sufficient, background hypotheses introduced by grain interaction modelling approaches.

# List of publications

## Peer-reviewed journal publications

- M. Ortolani, C. L. Azanza Ricardo, P. Scardi, “Measurement of stress factors and residual stress of a film by in situ X-ray diffraction during four-point bending”, *J. Appl. Cryst.* (2009), Vol. 42, Part 6, pages 1102-1109
- M. Ortolani, P. Scardi, C. L. Azanza Ricardo, “Analysis Of Residual Stress-Texture Relationships”, *Advanced Materials Research, THERMEC 2009 Supplement* (2010), Vol. 89-91, pages 425-430
- P. Scardi, M. Ortolani, M. Leoni, “WPPM: microstructural analysis beyond the Rietveld method”, *Materials Science Forum* (2010), Vol. 651, pages 155-171
- M. Ortolani, C. L. Azanza Ricardo, A. Lausi, P. Scardi, “Thin film stress and texture analysis at the MCX synchrotron radiation beamline at ELETTRA”, *Materials Science Forum* (2011), Vol. 681, pages 115-120
- M. Ortolani, C. Zanella, C. L. Azanza Ricardo, P. Scardi, “Elastic grain interaction in electrodeposited nanocomposite Nickel matrix coatings”, accepted for publication by *Surface and Coatings Technology* (doi: 10.1016/j.surfcoat.2011.10.056)
- M. Ortolani, C.L. Azanza Ricardo, A. Lausi, P. Scardi, “Stress gradients and grain interaction measurement in electrodeposited coatings by means of synchrotron radiation”, *Thin Solid Films* (2011), submitted

## **Congress participation**

- THERMEC 2009, August 25-29<sup>th</sup>, 2009, Berlin, Germany
- ECRS 8, June 26-28<sup>th</sup>, Riva del Garda (TN), Italy
- Size-Strain VI, October 17-20<sup>th</sup>, 2011, Presqu'île de Giens, Hyères, France

# Bibliography

- [1] M. Ohring. *Materials Science of Thin Films*. Academic Press, 2002.
- [2] R.J. Roe. Description of crystallite orientation in polycrystalline materials. (iii) general solution to pole figure inversion. *J. Appl. Phys.*, 36:2024–2031, 1965.
- [3] H.-J. Bunge. *Texture Analysis in Materials Science*. Butterworths, 1982.
- [4] I.C. Noyan and J.B. Cohen. *Residual Stress - Measurement by Diffraction and Interpretation*, Springer-Verlag. Springer-Verlag, 1987.
- [5] A. Guinier. *X-Ray diffraction In Crystals, Imperfect Crystals, and Amorphous Bodies*. W. H. Freeman and Company, 1963.
- [6] U. Welzel, J. Ligot, P. Lamparter, A. C. Vermeulen, and E. J. Mittemeijer. Stress analysis of polycrystalline thin films and surface regions by X-ray diffraction. *Journal of Applied Crystallography*, 38:1–29, 2004.
- [7] J. Stickforth. Über den Zusammenhang zwischen röntgenographischer Gitterdehnung und makroskopischen elastischen Spannungen. *Tech. Mitt. Krupp.*, 24:89–102, 1966.
- [8] H. Dölle and V. Hauk. Einfluss der mechanischen Anisotropie des Vielkristalls (Textur) auf die röntgenographische Spannungsermittlung. *Z. Metallkd.*, 69:410–417, 1978.
- [9] T. Mura. *Micromechanics of Defects in Solids*. Martinus Nijhoff Publishers, 1987.

- [10] F. Bollenrath, V. Hauk, and E. H. Müller. Zur Berechnung der vielkristallinen Elastizitätskonstanten aus den Werten der Einkristalle. *Z. Metallkd.*, 58:76–82, 1967.
- [11] A. Reuss. Berechnung der Fließgrenze von Mischkristallen auf Grund der Plastizitätsbedingung für Einkristalle. *Zeitschrift für angewandte Mathematik und Mechanik*, 9:49–58, 1929.
- [12] W. Voigt. *Lehrbuch der Kristallphysik*. Teubner (Leipzig, Berlin), 1910.
- [13] U. Welzel. *Diffraction Analysis of Residual Stress; Modeling Elastic Grain Interaction*. PhD thesis, Max-Planck-Institut für Metallforschung, Stuttgart, 2002.
- [14] S. Matthies and M. Humbert. On the Principle of a Geometric Mean of Even-Rank Symmetric Tensors for Textured Polycrystals. *J. Appl. Cryst.*, 28:254–266, 1995.
- [15] R. W. Vook and F. Witt. Thermally induced strains in evaporated films. *J. Appl. Phys.*, 36:2169–2171, 1965.
- [16] U. Welzel and S. Freour. Extension of the Vook-Witt and inverse Vook-Witt elastic grain-interaction models to general loading states. *Philosophical Magazine*, 87:3921–3943, 2007.
- [17] N Koch, U. Welzel, H. Wern, and E. J. Mittemeijer. Mechanical elastic constants and diffraction stress factors of macroscopically elastically anisotropic polycrystals: the effect of grain-shape (morphological) texture. *Philosophical Magazine*, 84:3547–3570, 2004.
- [18] R. J. Asaro and D. M. Barnett. The non-uniform transformation strain problem for an anisotropic ellipsoidal inclusion. *J. Mech. Phys. Solids*, 23:77, 1975.
- [19] A. Baczmanski, A. Tidu, P. Lipinski, M. Humbert, and K. Wierzbanski. New Type of Diffraction Elastic Constants for Stress Determination. *Materials Science Forum*, 524-525:235–240, 2006.
- [20] M. Ortolani, P. Scardi, and C. L. Azanza Ricardo. Analysis Of Residual Stress-Texture Relationships. *Advanced Materials Research, THERMEC 2009 Supplement*, 89-91:425–430, 2010.

## Bibliography

- [21] The GNU Scientific Library.
- [22] The Qt Framework.
- [23] G. G. Stoney. The Tension of Metallic Films Deposited by Electrolysis. *Proc. R. Soc. Lond.*, 82:172–175, 1909.
- [24] E. Eiper, K. J. Martinschitz, and J. Keckes. Combined elastic strain and macroscopic stress characterization in polycrystalline Cu thin films. *Powder Diffraction*, 21:25–29, 2006.
- [25] K. J. Martinschitz, E. Eiper, S. Massl, H. Köstenbauer, R. Daniel, G. Fontalvo, C. Mitterer, and J. Keckes. Rapid determination of stress factors and absolute residual stresses in thin films. *Journal of Applied Crystallography*, 39:777–783, 2006.
- [26] M. Ortolani, C. L. Azanza Ricardo, and P. Scardi. Measurement of stress factors and residual stress of a film by in situ X-ray diffraction during four-point bending. *Journal of Applied Crystallography*, 42:1102–1109, 2009.
- [27] K. F. Badawi, P. Villain, Ph. Goudeau, and P. O. Renault. Measuring thin film and multilayer elastic constants by coupling in situ tensile testing with x-ray diffraction. *Applied Physics Letters*, 80:4705–4707, 2002.
- [28] R. Delhez, Th. H. de Keijser, and E. J. Mittemeijer. *Surface Engineering*, 3:331–342, 1987.
- [29] M. Ortolani, C. L. Azanza Ricardo, A. Lausi, and P. Scardi. Stress gradients and grain interaction determination in electrodeposited coatings by synchrotron radiation. *Thin Solid Films*, submitted.
- [30] P. Scardi, S. Setti, and M. Leoni. Multicapillary optics for materials science studies. *Materials Science Forum*, 321-324:162–167, 2000.
- [31] M. Ortolani, C. L. Azanza Ricardo, P. Scardi, and A. Lausi. Thin film stress and texture analysis at the MCX synchrotron radiation beamline at ELETTRA. *Materials Science Forum*, 681:115–120, 2011.
- [32] NIST SRM 640c.

- [33] NIST SRM 660a.
- [34] Caglioti G., A. Paoletti, and F.P. Ricci. *Nucl. Instr.*, 3:223, 1958.
- [35] P. Scardi, Y.H. Dong, S. Setti, and V. Fontanari. A 4-point bending device for in situ measurement of elastic properties of polycrystalline materials by X-ray Diffraction. In *Proceedings of the 5th International Congress on Residual Stress*, volume 1, pages 67–73. IOM Communications, London, 2000.
- [36] C. Zanella. *Nanocomposite coatings produced by electrodeposition from additive-free bath: the potential of the ultrasonic vibrations*. PhD thesis, University of Trento, 2009.
- [37] J. W. Dini. *Electrodeposition: the materials science of coatings and substrates*. Noyes Publications, 1993.
- [38] N. Guglielmi. Kinetics of the deposition of inert particles from electrolytic baths. *J. Electrochem. Soc.*, 8:1009–1012, 1972.
- [39] N. Ibl, J.C. Puipe, and H. Angerer. *Surface and Coatings Technology*, 6:287, 1978.
- [40] N. Ibl. *Surface and Coatings Technology*, 10:81, 1980.
- [41] T. Manson. *Ultrasonics*, 24:245, 1986.
- [42] C. Zanella, M. Lekka, S. Rossi, and F. Deflorian. Study of the influence of sonication during the electrodeposition of nickel matrix nanocomposite coatings on the protective properties. *Corrosion Reviews*, in press.
- [43] J.P. Celis, J.R. Roos, and C. Buelens. A Mathematical Model for the Electrolytic Codeposition of Particles with a Metallic Matrix. *J. Electrochem. Soc.*, 13:1402, 1987.
- [44] J. Fransaer, J.P. Celis, and J.R. Roos. Analysis of the Electrolytic Codeposition of Non-Brownian Particles with Metals. *J. Electrochem. Soc.*, 139:413, 1992.
- [45] J. K. Luo, M. Pritschow, A. J. Flewitt, S. M. Spearing, N. A. Fleck, and W. I. Milne. Effects of Process Conditions on Properties of Electroplated Ni Thin



## Bibliography

- Films for Microsystem Applications. *Journal of The Electrochemical Society*, 153:D155–D161, 2006.
- [46] S.E. Hadian and D.R. Gabe. Residual stresses in electrodeposits of nickel and nickel-iron alloys. *Surface and Coatings Technology*, 122:118–135, 1999.
- [47] L. Benea, P. L. Bonora, A. Borello, and S. Martelli. Wear corrosion properties of nano-structured SiC-nickel composite coating obtained by electroplating. *Wear*, 249:995–1003, 2002.
- [48] C. B. Nielsen, A. Horsewell, and M. J. L. Østergård. On texture formation of nickel electrodeposits. *Journal of Applied Electrochemistry*, 27:839–845, 1997.
- [49] R. P. Socha, P. Nowak, K. Laajelehto, and V. Juhani. Particle-electrode surface interaction during nickel electrodeposition from suspensions containing SiC and SiO<sub>2</sub> particles. *Colloids and Surfaces A*, 235:45–55, 2004.
- [50] M. Ortolani, C. Zanella, C. L. Azanza Ricardo, and P. Scardi. Elastic grain interaction in electrodeposited nanocomposite Nickel matrix coatings. *Surface and Coatings Technology*, accepted.
- [51] P. Scardi and M. Leoni. Line profile analysis: pattern modelling versus profile fitting. *Journal of Applied Crystallography*, 39:24–31, 2006.
- [52] P. Scardi, M. Ortolani, and M. Leoni. WPPM: microstructural analysis beyond the Rietveld method. *Materials Science Forum*, 651:155–171, 2010.
- [53] L. E. Alexander. *X-ray Diffraction Procedures: For Polycrystalline and Amorphous Materials*. J. Wiley & Sons, 1974.
- [54] F. Attar and T. Johannesson. Adhesion and X-ray elastic constant evaluation of CrN coating. *Thin Solid Films*, 258:205–212, 1995.
- [55] A. V. Dobrynin. On the applicability of Stoney’s formula for calculating the mechanical stresses in thick films and coatings. *Technical Physics Letters*, 23:709–710, 1997.
- [56] F. Ebrahimi, G. R. Bourne, M. S. Kelly, and T.E. Matthews. Mechanical properties of nanocrystalline nickel produced by electrodeposition. *Nanostructured Materials*, 11:343–350, 1999.

- [57] E. Eiper, K. J. Martinschitz, J. W. Gerlach, J. M. Lackner, I. Zizak, N. Darowski, and J. Keckes. X-ray elastic constants determined by the combination of  $\sin^2\psi$  and substrate-curvature methods. *Z. Metallkd.*, 96:1069–1073, 2005.
- [58] A.M. El-Sherik, J. Shirokoff, and Erb U. Stress measurements in nanocrystalline Ni electrodeposits. *Journal of Alloys and Compounds*, 389:140–143, 2005.
- [59] S. Huang and X. Zhang. Extension of Stoney formula for film-substrate systems with gradient stress. *Journal of Micromechanics Microengineering*, 16:382–389, 2006.
- [60] M. O. Kostin and O. H. Sheikina. Microstructure and Mechanical Properties of Electrodeposited thin Nickel Films. *Materials Science*, 38:898–902, 2002.
- [61] P. Lamparter, A. C. Vermeulen, E. J. Mittemeijer, U. Welzel, and J. Ligot. Stress analysis of polycrystalline thin films and surface regions by X-ray diffraction. *Journal of Applied Crystallography*, 38:1–29, 2005.
- [62] A. Lausi, E. Busetto, M. Leoni, and P. Scardi. The MCX project: a powder diffraction beamline at ELETTRA. *Synchrotron Radiation in Natural Science*, 5:100–104, 2006.
- [63] M. Leoni, P. Scardi, and S. Setti. Multicapillary optics for materials science studies. *Materials Science Forums*, 321-324:162–167, 2000.
- [64] M. Ortolani. Thin film mechanical properties by X-ray diffraction during in-situ four-point bending. Master’s thesis, University of Trento, 2007.
- [65] J. Roos, J.P. Celis, J. Franssaer, and C. Buelens. *Journal of the Minerals, Metals & Materials Society*, 1990.
- [66] C. Sarioglu. The effect of anisotropy on residual stress values and modification of Serruys approach to residual stress calculations for coatings such as TiN, ZrN and HfN. *Surface & Coatings Technology*, 201:707–717, 2006.
- [67] V. S. Speriosu, A. Segmüller, and I. C. Noyan. X-ray diffraction studies of thin films and multilayer structures. *Scripta Materialia*, 288:231–234, 2006.






*Bibliography*

- [68] M. R. Vaezi, S. K. Sadrnezhad, and L. Nikzad. Electrodeposition of Ni-SiC nano-composite coatings and evaluation of wear and corrosion resistance and electroplating characteristics. *Colloids and Surfaces A*, 315:176–182, 2008.
- [69] M. Wilkens. Density and Distribution of Dislocations. *Phys. Stat. Sol. A*, 2:359–370, 1970.
- [70] Y.H. Yu, M.O. Lai, L Lu, and G.Y. Zheng. Measurement of in-plane elastic constants of crystalline solid films by X-ray diffraction coupled with four-point bending. *Surface & Coatings Technology*, 200:4006–4010, 2006.
- [71] C. Zanella, M. Lekka, A. Lanzutti, and P. L. Bonora. Influence of the particle size on the mechanical and electrochemical behaviour of microand nano-nickel matrix composite coatings. *Surface Engineering*, 39:31–38, 2009.
- [72] Z. Zhong, C. Kao, D. P. Siddons, H. Zhong, and J. B. Hastings. A lamellar model for the X-ray rocking curves of sagittally bent Laue crystals. *Acta Crystallographica*, 59:1–6, 2003.

*Bibliography*

## Appendix A

# QXrdTex user manual

The QXrdTex software package was conceived with programmability in mind. Its interface may be described as a script editor, supporting syntax highlighting and code snippets; on top of basic functions (such as  Open,  Save, or  Find), script execution control is provided by means of the Run () and Stop () button; the latter is provided to force execution stop, and should be avoided in most cases.

The application digests a Javascript input, in order to execute a batch of operations. Text output is returned in a box at the bottom of the main window, whereas plots appear on the right side. Several custom objects have been implemented into the Javascript engine, offering a complete set of tools for X-ray stress data analysis.

Data is provided in the form of text files; once data files have been prepared, the engine may be instructed to load the data providing a complete path to the data files.

This Appendix is divided in two parts, describing data files format and custom script objects respectively.

### A.1 Data files

Files format was conceived to contain a set of data in the form of one or more tables. Generally, data is preceded by custom tags, that provide additional information or identification to following tables. Data files may contain comments, for the user's

reference, that will be ignored when reading data from the file; comments start with a sharp (#) symbol and last until the end of the line; spacing is usually irrelevant, unless otherwise specified. Files accepted as input by the program are hereby briefly presented.

**Orientation Distribution Function data** Numerical ODF data can be loaded from file, using the command `new OdfData (<unit_cell>, <path_to_file>)`. More information is available in the following Section. Data should be arranged in the form of a list of  $f$  values, ordered by increasing  $\alpha$ ,  $\beta$  and  $\gamma$  (in this order).

The file needs a header preceding the data table, that specifies the number of points to be read, and symmetry multipliers if needed. The first line should contain the label `ODF 1.0`, in order to identify the contents of the file. It is followed by a line that contains a description of the material it refers to. Finally, the number of data points per angle and corresponding symmetry multiplier is to be provided. A complete header looks like this:

```
ODF 1.0
a sample ODF
alpha 1 1
beta 91 2
gamma 91 4
```

It reads as follows: the file contains ODF data for “a sample ODF”. Sample possesses fibre texture, so the ODF is independent on  $\alpha$ ; hence, only one point along the  $\alpha$  axis is provided, with no symmetry multiplier required. One point per degree (for a total of 91, including extremes) is provided along the  $\beta$  and  $\gamma$  axes, respectively; as data is only provided in the  $[0^\circ, 90^\circ]$  range, the corresponding symmetry multipliers to cover all of Euler space should be 2 and 4, respectively.

Data should follow in the form of a list of  $f$  values; it may be convenient to arrange it in the form of a table for better viewing, although the program is insensitive to data formatting within the file.

**XRD stress measurement data file** XRD stress measurements can be loaded from a file that contains one or more “ $\sin^2 \psi$ ” tables, whose entries should be in the

### A.2. Custom classes

form of  $(\psi, 2\theta)$  pairs (in degrees). Tables are preceded by a header that indicates what  $hkl$  index they refer to, and what  $\phi$  rotation they were collected at.

The file header should contain a “XrdStressMeasurements 1.0” label, identifying the file content; following, the number of “ $\sin^2 \psi$ ” tables, and a list of  $hkl$  indices. It is also possible to indicate whether measurements were collected at  $\phi = 0^\circ$  only, or at  $\phi = 90^\circ$  as well; finally, confidence levels for  $2\theta$  positions may be provided, to be used as weight in the least squares minimisation. A complete header looks like this:

```
XrdStressMeasurements 1.0
peaks 2
1 1 1
2 0 0
psiCount 1
errors yes
```

The above header indicates that the data file contains strain data measured on two reflections (111 and 200); that measurements were only performed at  $\phi = 0^\circ$  (`psiCount 1`) and that data is provided with confidence bands.

Following, each “ $\sin^2 \psi$ ” table should be entered, preceded by a parameter indicating the number of  $\psi$  points, in the following form:

```
psiCount 10
0.0 44.502 0.002
6.0 44.518 0.004
12.0 44.523 0.003
...
```

## A.2 Custom classes

Several custom classes were implemented. Many act as QObject-based [22], C++ wrappers to GSL [21] objects, that were originally introduced to implement modelling algorithms in a more efficient way, and were then made available to the script engine. Several more classes were then added to handle physical data, such as unit

cell information and elastic tensor representations; these objects are collected in a separate Section.

### A.2.1 Generic-purpose classes

This Section introduces the generic-purpose classes that are available within the script engine. They are presented separately because they do not specifically concern handling physical material data, but rather provide a set of standard templates to handle mathematical objects, such as vectors, matrices and linear system solvers.

**Vector** This class handles a vector of real values; length must be specified upon allocation.

`new Vector (n)` allocates a new vector of length *n*

`count ()` returns the length of the vector

`at (position)` returns the item at *position*

`setAt (position, value)` sets *value* at *position*

`copyFrom (vector)` copies all items of vector

`copyTo (vector)` copies all items into *vector*

`compareElements (vector)` returns *true* if all items are equal to *vector*'s

`setAll (value)` sets all items to *value*

`setZero ()` sets all items to zero

`setBasis (index)` sets all items to zero, except for *index*, which is set to one

`add (vector)` adds *vector*'s content itemwise

`scale (value)` scale all items by *value*

`storeSum (vector_1, vector_2)` stores here the sum of *vector\_1* and *vector\_2*

`product (vector)` returns the dot product with *vector*

`storeProduct (matrix, vector)` stores here the product of *matrix* with *vector*



## A.2. Custom classes

**Matrix** This class handles a matrix of real values; size must be specified upon allocation.

`new Matrix (m, n)` allocates a new matrix of size  $n \times m$

`rows ()` returns the number of rows

`columns ()` returns the number of columns

`at (i, j)` returns the item at  $(i,j)$

`setAt (i, j, value)` sets *value* at  $(i,j)$

`copyFrom (matrix)` copies all items of *matrix*

`copyTo (matrix)` copies all items into *matrix*

`copyRowFrom (i, vector)` copies *vector* into row *i*

`copyRowTo (i, vector)` copies row *i* into *vector*

`copyColumnFrom (i, vector)` copies *vector* into column *i*

`copyColumnTo (i, vector)` copies column *i* into *vector*

`compareElements (matrix)` returns *true* if all items are equal to *matrix*'

`setAll (value)` sets all items to *value*

`setZero ()` sets all items to zero

`setIdentity ()` sets all items to zero, diagonal items to one

`transpose ()` transposes content

`add (matrix)` adds *matrix*' content itemwise

`scale (value)` scale all items by *value*

`storeSum (matrix_1, matrix_2)` stores here the sum of *matrix\_1* and *matrix\_2*

`storeProduct (matrix_1, matrix_2)` stores here the product of *matrix\_1* and *matrix\_2*

**Pattern** Handles a resizable list of  $(x, y, \Delta y)$  values;  $\Delta y$  is optional. Used for interpolation and plotting.

`new Pattern ([x, y, [err]])` allocates a new pattern; if provided, fills content with *x*, *y*, *err*

`x, y, err (i)` returns *x*, *y*, *err* value at *i*

`count ()` returns the number of entries

`append (x, y [, err])` appends a new entry at the end

`count ()` clears all entries

`copyFrom (pattern)` copies the content of *pattern*

`saveToFile (path)` saves entries into a text file specified in *path*; overwrites the file, if already present

`minX, maxX, minY, maxY ()` returns minimum and maximum *x* or *y* values

**LinearSolverLU** Handles a LU solver; used for solving linear systems or for matrix inversion.

`new LinearSolverLU (n)` allocates a solver for a system of dimension *n*

`decompose (matrix)` computes the LU decomposition of *matrix*

`solve (x, b)` solves  $Ax = b$ , needs *A* to be LU-decomposed first

`invert (matrix)` computes the inverse of the LU-decomposed matrix and stores the result into *matrix*

`determinant ()` computes the determinant of the LU-decomposed matrix

**Interpolation** Computes an interpolation of any given pattern.

`new Interpolation (pattern, type)` initialises interpolation of *pattern*; *type* can be Linear, Polynomial, CubicSpline, CubicSplinePeriodic, Akima, AkimaPeriodic

## A.2. Custom classes

`evaluate (x)` evaluates interpolation value at point  $x$

`evaluateDerivative (x)` evaluates interpolation derivative value at point  $x$

`evaluateIntegral (x1, x2)` evaluates interpolation finite integral between  $x1$  and  $x2$

**FitLinear** Computes a linear, least-squares fit of data in any given pattern.

`new Interpolation (pattern)` initialises least-squares fit of *pattern*

`solve ()` computes least-square solution

`coefficients ()` returns calculated linear function parameters in the form of a vector

`covariance ()` returns the covariance matrix

`degreesOfFreedom ()` returns the number of degrees of freedom

`normalizedChiSquare ()` returns the normalised  $\chi^2$  of the minimisation

**PlotCurve** Handles pattern representation on a  $xy$  plot.

`new PlotCurve ()` initialises the object

`setPattern (pattern)` indicates that data contained in *pattern* should be represented

`setSymbol (symbol, size, border_color, fill_color)` specify what *symbol* to use for data points; options are NoSymbol, Square, Circle; *size* of symbol is in pixels; *colors* are represented by a string, such as “black”, “red”, “blue”

`setSymbol (line, thickness, color)` specify what *line* style to use for connecting data points; options are NoLine, Continuous, Dashed; *thickness* is in pixels; *color* is represented by a string

`setErrorBar (type, color)` specify what *type* of error bar to display; options are NoErrorBar, LineBar; *color* is a string representation

PlotCurve objects are displayed on screen by means of the global object Plot.

**Plot (global object)** Displays curves in a *xy* plot. This is a global object, that may be invoked directly rather than allocated on a per-need basis.

`add (title, plot_curve)` adds a tab labelled *title* to the plot window, if not already present; displays *plot\_curve* in the corresponding tab

**Print (global function)** This function is used to display custom text output in the bottom window. Accepts any number of arguments, and about any argument type that can be represented in the form of simple text.

## A.2.2 Physical data manipulation classes

These custom classes were implemented to handle physical material data. The user is supposed to primarily interact with this kind of objects.

**UnitCell[*type*]** Describes a crystalline unit cell; *type* can be Cubic, Hexagonal or Triclinic (generic).

`new UnitCell[type] (a, b, c, alpha, beta, gamma)` initialises the unit cell; for a cubic system, only *a* is required; for a hexagonal one, *a* and *c*; all arguments are required for a triclinic system

`a, b, c, alpha, beta, gamma ()` returns the corresponding unit cell parameter

**Ihkl** Represents a triad of Miller indices, indicating a crystallographic plane or direction.

`new Ihkl (h, k, l)` initialises the descriptor

`h, k, l ()` returns the corresponding index

**ElasticTensor** Describes an elastic tensor; information is stored both in terms of stiffness and compliance.

`new ElasticTensor ()` initialises the object; does not store any actual data yet

## A.2. Custom classes

`initializeCubicS` ( $S_{11}$ ,  $S_{12}$ ,  $S_{44}$ ) initialises entries for a cubic symmetry from compliance elements

`initializeCubicC` ( $C_{11}$ ,  $C_{12}$ ,  $C_{44}$ ) initialises entries for a cubic symmetry from stiffness elements

`initializeHexagonalS` ( $S_{11}$ ,  $S_{12}$ ,  $S_{13}$ ,  $S_{33}$ ,  $S_{44}$ ) initialises entries for a hexagonal symmetry from compliance elements

`initializeHexagonalC` ( $C_{11}$ ,  $C_{12}$ ,  $C_{13}$ ,  $C_{33}$ ,  $C_{44}$ ) initialises entries for a hexagonal symmetry from stiffness elements

`initializeFromS` ( $S$ ) initialises entries from a generic matrix representation of compliance

`initializeFromC` ( $C$ ) initialises entries from a generic matrix representation of stiffness

`storeS` ( $S$ ) stores compliance into  $S$

`storeC` ( $C$ ) stores stiffness into  $C$

**OdfData** Handles Orientation Distribution Function data. Provides capability to load from file as well as normalise over the Euler space.

`new OdfData` ( $cell$ ,  $path$ ) initialises the object, loading data from file at  $path$ ; crystalline unit cell  $cell$  needs to be provided for symmetry evaluation purposes

`value` ( $g$ ) returns value at  $\mathbf{g} = (\alpha, \beta, \gamma)$

`integrate` () returns the integral over the whole Euler space; after normalisation, it should return  $8\pi^2$

`normalize` () normalizes enforcing the integral over the whole Euler space to be  $8\pi^2$

**Model**[*name*] Computes X-ray and macroscopic elastic constants based on a grain interaction model, single crystal elastic properties, and texture information. *Name* can be Reuss, Voigy, VookWitt, InverseVookWitt, Eshelby, Baczmanski.

`new Model`[*name*] (*cell*, *odf*, *elasticTensor* [, *eta1*, *eta2*]) initialises the model for the given unit *cell*, *ODF* data and single crystal *elastic tensor*; morphological texture models (Eshelby, Baczmanski) require grain aspect ratios *eta1* and *eta2* to be specified as well

`evaluateConstants` (*a*) fills vector *a* with macroscopic elastic constants  $S_1$  and  $1/2S_2$

`evaluateStressFactors` (*f*, *hkl*, *psi*, *phi*) calculates X-ray stress factors  $F_{11}$  and  $F_{22}$  and stores the result into vector *f*; requires *hkl* and sample rotation angles *psi* and *phi*, in degrees

**StressModel** Performs residual stress data analysis, with the given grain interaction model(s).

`new ElasticTensor` () initialises the object

`loadMeasurementsFromFile` (*path*) loads data from file at *path*

`addModel` (*model*, *fraction*) adds a grain interaction *model* to minimisation; material volume *fraction* obeying to the *model*'s behaviour may be specified

`clearModels` () clears the list of grain interaction models for minimisation

`measurements` () returns the number of “ $\sin^2 \psi$ ” data sets

`measurementIhklString` (*i*) returns a string representation of the *hkl* index used in the *i*-th measurement; useful for plotting and reporting purposes

`setWavelength` (*lambda*) sets the radiation wavelength used for experimental measurements

`set`[*Parameter*] (*value*, *fixed*) sets the initial guess for *parameter* (Cell for unit cell parameter(s); DeltaTth for a global  $2\theta$  error (in degrees); DeltaPsi for a global  $\psi$  tilt error (in degrees); StressPlane for  $\sigma_{\parallel}$ ; StressLong for an additional  $\sigma_{11}^S$  stress component)

### A.3. Example script

`solve ()` performs least-squares minimisation with the given initial conditions

`[Parameter] ()` returns the value of a minimisation *parameter* (cellA, C, ... for unit cell parameters; deltaTth, deltaPsi, stressPlane, stressLong represent the same quantities introduced before)

`[Parameter]Err ()` returns an estimated standard deviation for *parameter*

`patterns (data, fit, i, p)` fills patterns *data* and *fit* with experimental points and modelling, for the *i*-th “ $\sin^2 \psi$ ” data set and direction  $\phi = 0^\circ$  (p=0) or  $\phi = 90^\circ$  (p=1); output data points are arranged as  $(\sin^2 \psi, d_{hkl})$  pairs. This function is used for plotting

## A.3 Example script

The use of this application is better explained with a practical example. A typical script for X-ray stress analysis is hereby presented and commented step-by-step; it describes the problem of residual stress evaluation in a polycrystalline electrodeposited Nickel coating.

First, the known physical parameters for the sample material are entered: the unit cell parameter and single crystal elastic constants.

```
var cell = new UnitCellCubic (3.524) // [Angstrom]
var elasticConstants = new ElasticConstants
elasticConstants.initializeCubicS (7.95, -2.65, 8.61) // [1/TPa]
```

The ODF data is then loaded; normalisation is performed.

```
var odf = new OdfData (cell, "~/galvanic Nickel ODF.txt")
odfSim.normalize()
```

The stress analysis is now initialised; data is loaded from a file.

```
var stressAnalysis = new StressModel()
stressAnalysis.loadMeasurementsFromFile ("~/galvanic Nickel strain data.txt")
```

Grain interaction models are appended to the analysis: for this example we are only using the simple Reuss and Voigt descriptions. The software will calculate the best-fitting Hill mixing parameter.

```
stressAnalysis.addModel (new ModelReuss (cell, odfSim, elasticConstants),
0.5)
stressAnalysis.addModel (new ModelVoigt (cell, odfSim, elasticConstants),
0.5)
```

Minimisation parameters are initialised (and set free to vary during iterations).

```
stressAnalysis.setCell (cell, false)
stressAnalysis.setWavelength (1.540665) // Cu K alpha, [Angstrom]
stressAnalysis.setStressPlane (180) // [MPa]
stressAnalysis.setDeltaTth (0.0, false) // [degrees]
```

Perform minimisation.

```
stressAnalysis.solve()
```

Finally, display the results in plots.

```
for (var i = 0; i < stressAnalysis.measurements(); i++) {
var curvePoints = new PlotCurve, curveFit = new PlotCurve
curvePoints.setLine (PlotCurve.NoLine)
curvePoints.setSymbol (PlotCurve.Circle, 6, "black")
curveFit.setLine (PlotCurve.Continuous, 2, "red")
curveFit.setSymbol (PlotCurve.NoSymbol)
// Data points will be shown as black dots;
// modelling as a red line
var dataPoints = new Pattern, dataFit = new Pattern
stressAnalysis.patterns (dataPoints, dataFit, i, 0) // retrieve pattern
data from the minimisation object
curvePoints.setPattern (dataPoints); curveFit.setPattern (dataFit)
// data points are assigned to their corresponding
// curves, which can now be displayed
Plot.add (stressAnalysis.measurementIhklString(i), curvePoints)
Plot.add (stressAnalysis.measurementIhklString(i), curveFit)
// use the measurement hkl as plot tab label
}
```

The final result is shown below (Figure A.1).



### A.3. Example script

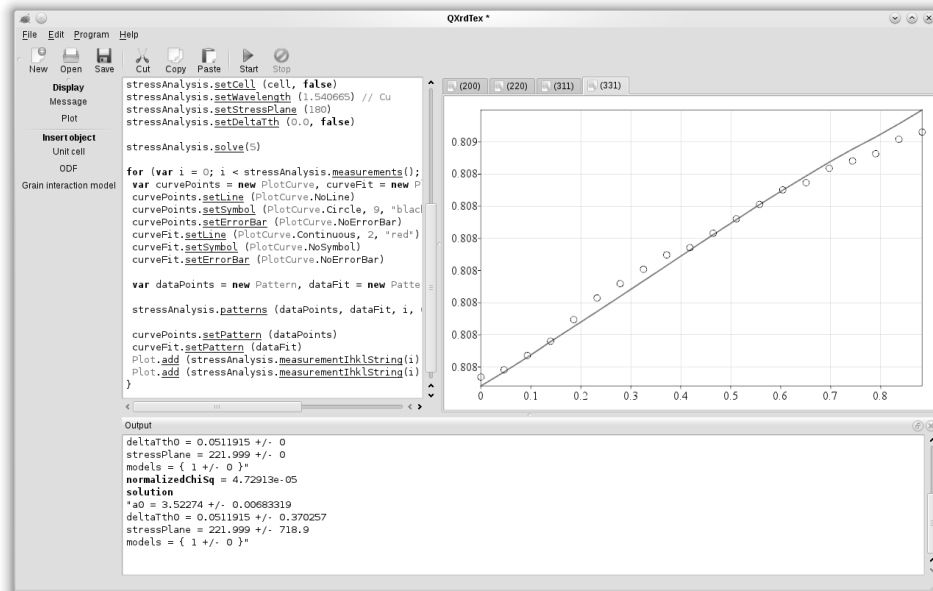


Figure A.1: Example stress analysis with QXrdTex.

*Appendix A. QXrdTex user manual*

# Acknowledgments

I would like to thank professor Paolo Scardi and Dr. Matteo Leoni for their invaluable support and advising; and Cristy Azanza for sharing my headaches over instrumental setup and data analysis. Thanks for their assistance with experiments to Dr. Mirco D’Incau (UniTN), and Dr. Andrea Lausi with his team (Elettra).

Special thanks to my friends and colleagues, and my students, for their friendship and help; to my current employers and new co-workers at Tenaris Dalmine, for their support and acknowledgment, and for all study permits allowed to attend this Doctorate School.

A very special thank to my parents Cesare and Emanuela; to my closest relatives; and to our animals, for all their affection and support through the course of this academic adventure.